Journal of Structural Geology 33 (2011) 519–536

Contents lists available at ScienceDirect

Journal of Structural Geology

journal homepage: www.elsevier.com/locate/jsg

Scaling and geometric properties of extensional fracture systems in the proterozoic basement of Yemen. Tectonic interpretation and fluid flow implications

Edouard Le Garzic [a,*], Thibaut de L'Hamaide [b], Marc Diraison [a], Yves Géraud [a], Judith Sausse [c], Marc de Urreiztieta [d,e], Benoît Hauville [d], Jean-Michel Champanhet [d]

[a] Institut de Physique du Globe de Strasbourg, IPGS – UMR 7516, CNRS et Université de Strasbourg (EOST), 1 rue Blessig, 67084 Strasbourg Cedex, France
[b] TTI Production, 2 avenue P. Angot, Technopole Helioparc, 64000 Pau, France
[c] Nancy Université, Département des Sciences de la Terre, UMR CNRS 7566 G2R, BP239, 54506 Vandoeuvre les Nancy, France
[d] Total E&P Yemen, P.O. Box 842, Sana'a, Republic of Yemen
[e] Petronas Carigali SDN. BHD., Petronas Twin Towers, Kuala Lumpur City Centre 50088, Malaysia

ARTICLE INFO

Article history:
Received 19 July 2010
Received in revised form
21 January 2011
Accepted 28 January 2011
Available online 4 February 2011

Keywords:
Crystalline basement
Fractured reservoir
Distribution law
Hierarchical fault zones geometry
Dual porosity model
Fluid flow

ABSTRACT

Multi-scale mappings of fracture systems in the crystalline basement of Yemen are presented. Fracture datasets are described through statistical analyses of direction, length, spacing, density, and spatial distribution. Results are combined with field observations and can be directly used to model the geometry of the fracture networks in analog basement rocks, from multi-kilometric to decametric scales. The fractured reservoir analog is defined with a dual porosity model in which tectonic and joint systems correspond to the basement reservoir "backbone" and "matrix" respectively. These two end-members reveal contrasting geometrical, reservoir, and scaling properties. In tectonic systems, multi-scale geometries are "self-similar", the fracture network shows fractal behavior (power-law length distribution and clustered spacing), and fault zones show hierarchical organization of geometrical parameters such as length, thickness, and spacing. In joint systems, the fracture network is scale dependent with exponential length distribution, and shows anti-clustered spacing. However, these two end-members have both well-connected properties, with fault zones acting as main drain and joint systems acting as the fluid supply.

1. Introduction

Recent development of basement fractured reservoirs "in and around igneous rocks" for both oil exploration and geothermal industries have been carried out in recent years (Schutter, 2003). The nature of basement fractured reservoirs implies different exploration and production strategies compared with conventional sedimentary ones. Most of the time, available data are restricted to multiple 1-D datasets (i.e. borehole data including cores, Formation MicroImager (FMI), wireline…) that are difficult to correlate from well to well when attempting to construct a realistic 3-D model of reservoir. Analyses of field rock analogs are thus required for a better understanding of the fracture system geometry. The nature and evolution of the fracture systems have direct influences on the fluid flow pathways in low permeability crystalline rocks. As a consequence, the geometrical attributes characterizing the fracture systems such as orientation, length, spacing, spatial distribution and connectivity have to be well constrained. A key point is the correct understanding of the scaling characteristics of different types of fracture systems, which could guide both the interpretation of regional data and its extrapolation to other different scales. In addition, quantitative characterization of the spatial distribution of fault zones are needed to better understand hierarchical organization of structural blocks and the role of fault zones in compartmentalizing fields.

The characterization of fractured basements, particularly in crystalline rocks, remains poorly documented by field examples. However, some authors such as Genter and Castaing (1997), Escuder Viruete et al. (2001), McCaffrey et al. (2003) and Sanders et al. (2003) have proposed statistical descriptions of natural fracture networks occurring in various environments. Several parameters were studied, mainly the spacing, the fault zone thickness and the length distributions of fractures. Velde et al. (1991) characterized the fractal distribution of fracture patterns in granites. Gillespie et al. (1993) compared different types of statistical and geometrical methods for the characterization of the spatial distribution of fractures in 1, 2 and 3D. Other contributions based on natural fracture set studies in

* Corresponding author. Fax: +33 3 68 85 04 02.
E-mail address: edouard.le-garzic@illite.u-strasbg.fr (E. Le Garzic).

0191-8141/$ – see front matter © 2011 Elsevier Ltd. All rights reserved.
doi:10.1016/j.jsg.2011.01.012

granites show that the connectivity of the fracture systems is characterized by a statistical law deduced from the fracture extension distributions and the fact that fluids follow preferential pathways within a fracture network (Long and Witherspoon, 1985; Ledésert et al., 1993a, 1993b; Bour and Davy, 1997; Bour et al., 2002). A number of laws are commonly cited to characterize the statistical distribution of a fault zone property, as well as the type of rock fragmentation, its development and its maturity. Generally, log-normal, exponential negative or power-law distributions prevail in the literature (Bonnet et al., 2001).

In this study, the scaling properties of an extensional fracture system from the proterozoic basement of Yemen are described for scale studies from meters to pluri-kilometers. The statistical properties of the fracture network are described through series of fracture trace maps at different scales that are derived from satellite imagery interpretation combined with field observations. In a first step, inspection of structural maps combined with statistical analyses allows us to propose a tectonic model for formation of each fracture set. In a second step, a multi-scale model of the fracture network is proposed and discussed. These results provide insights concerning the mechanisms of fracture formation, fluid movement through the fracture network and reactivation of pre-existing fracture systems. Two types of fracture organization are proposed: some major fault zone network and some micro-block fracture systems are finally discussed and extrapolated to the reservoir-scale.

2. Regional settings

The present configuration of the Arabian-Nubian Shield results from the accretion of low-grade island arcs terranes and high-grade continental terranes during the Pan-African orogeny (Fig. 1). These collision events occurred from ~750 to ~600 Ma (Stoeser and Camp, 1985; Al-Saleh et al., 1998; Blasband et al., 2000; Meert, 2003), and gave rise to N–S to NE–SW trending suture zones (Fig. 1). The final stage of the Pan-African orogeny is characterized by a widespread phase of NW–SE extension and by the development of lithospheric NW–SE trending faults with left-lateral strike-slip, named the Nadj Fault system (Fig. 1).

At the end of the Jurassic and the beginning of the Cretaceous, separation between India-Madagascar plate and African-Arabian margin (i.e. Somoma Ocean opening) induced reactivation of the inherited Nadj Fault system and development of extensive basins (Redfern and Jones, 1995; Birse et al., 1997). The three major Jurassic and Cretaceous extensive basins of Yemen, from West to East, are the Marib-Shabwah-Hajar basin, the Say'un Al Masilah basin and the Jiza-Qamar basin (Fig. 1). The geometry and sedimentary filling of these Mesozoic basins vary spatially and temporally from West to East (Bosence, 1997). The Marib-Shabwah-Hajar basin, with the main strike NW–SE, follows the Nadj trend of the Precambrian basement (Redfern and Jones, 1995; Birse et al., 1997), and its syn-rift filling is early Kimmeridgian to Thitonian in age (Ellis et al., 1996; Holden and Kerr, 1997). Toward the East, Say'un Al Masilah basin and Jiza-Qamar basin are progressively oriented more East-West, and rifting initiation becomes younger, with Kimmeridgian to early Cretaceous subsidence for the Say'un Al Masilah basin, and with Hauterivian to Paleogene subsidence for Jiza-Qamar basin (Redfern and Jones, 1995; Beydoun et al., 1996; Bosence, 1997).

The opening of the Gulf of Aden was the latest major tectonic event occurring in the studied area. It is a young oceanic basin located between the Arabian and the Nubia-Somalia plate (Fig. 1). Its principal characteristic is the low angle between the general axis rift orientation (N075°E) and spreading direction (N030°E). These features are consistent with an oblique rifting configuration (Manighetti et al., 1997; Dauteuil et al., 2001). Syn-rift filling recorded along the northern margin was deposited between 35 Ma and 20 Ma (Watchorn et al., 1998), while spreading started at 17,6 Ma (Leroy et al., 2004; d'Acremont et al., 2006). Onshore structures related to the opening of Gulf of Aden are complex. Several basins oriented parallel to the coast (~N075°E) were formed during the Oligocene, and the two major ones are the Aden-Abyan and Mukalla-Sayhut basins (Fig. 1). Oligocene extension was also intensively controlled by the reactivation of pre-existing structures related to Mesozoic basins (Khanbari, 2000; Huchon and Khanbari, 2003; Bellahsen et al., 2006). The Bahlaf graben, in prolongation of the Marib-Shabwah-Hajar basin, and the Jiza-Qamar basin are major reactivating structures of the Yemen margin (Brannan et al., 1997; Huchon and Khanbari, 2003 and references therein).

3. Zone of study

The Mukalla proterozoic basement is located in the south-east edge of the Mukalla horst, in the linking zone between the Marib-Shabwah-Hajar basin and the Mukalla-Sayut basin (Fig. 1). A geological map of the Mukalla basement area (Fig. 2) was constructed by integration of existing maps (GDR-surveying team and the Department of Geology & Mineral Exploration/Aden, 1987), an existing field study (Huchon and Khanbari, 2003), our own field survey, a satellite imagery interpretation (Aster and Landsat) and a Digital Elevation Model (DEM) interpretation (SRTM 90 m). The basement area chosen for satellite analysis is located in the central zone of this map and is bounded by E–W and NW–SE trending regional fault zones (Fig. 2).

The Mukalla basement corresponds to a volcano-sedimentary complex which is mainly composed of basic rocks related to a back-arc basin system. This volcano-sedimentary complex (undifferentiated basement on Fig. 2) is intruded by several late Pan-African granitoids, as the Burum granite. Detailed structural analysis was focused on this Burum granite because granite texture fits much better than a complex association of volcanic and sedimentary rocks to the structural map produced by satellite imagery analysis.

4. Terminology and typology of structures observed in the field

A fracture is an approximately planar discontinuity such as joints, faults, dykes or veins (Peacock et al., 2000). For the purpose of this study, we have classified fractures into two main groups: primary and secondary fractures. On the one hand, we consider primary fractures as all discontinuities developed during emplacement, cooling and decompression of the magma (Price and Cosgrove, 1990; Sanders et al., 2003), like joints, diaclases or aplitic/pegmatitic dykes. On the other hand, secondary fractures result from tectonic forces and correspond to faults and related fractures. In order to clarify description and interpretation of structures through this manuscript, all the terms used in this paper are each described in this section. Definitions and descriptions of terms such as joint, fault zone, damage zone or fracture corridor are based on published data and own field observations realized in the Burum granite.

4.1. Primary fractures and protolith concept

Primary fractures are fractures formed during emplacement, cooling and decompression of the magma in the upper crust. These structures are predominant outside the main deformation zones and consist of several typical sets of joints: flat-lying joints, sub-vertical orthogonal joints sets, and another joint set often oblique with a dip angle near 45° (Fig. 3c). Each set rarely presents clusters of fractures and is mostly regularly or randomly spaced. In the Burum granite, these sets are often unmineralized even if aplitic or pegmatitic veins are sometimes observed. The primary fractures

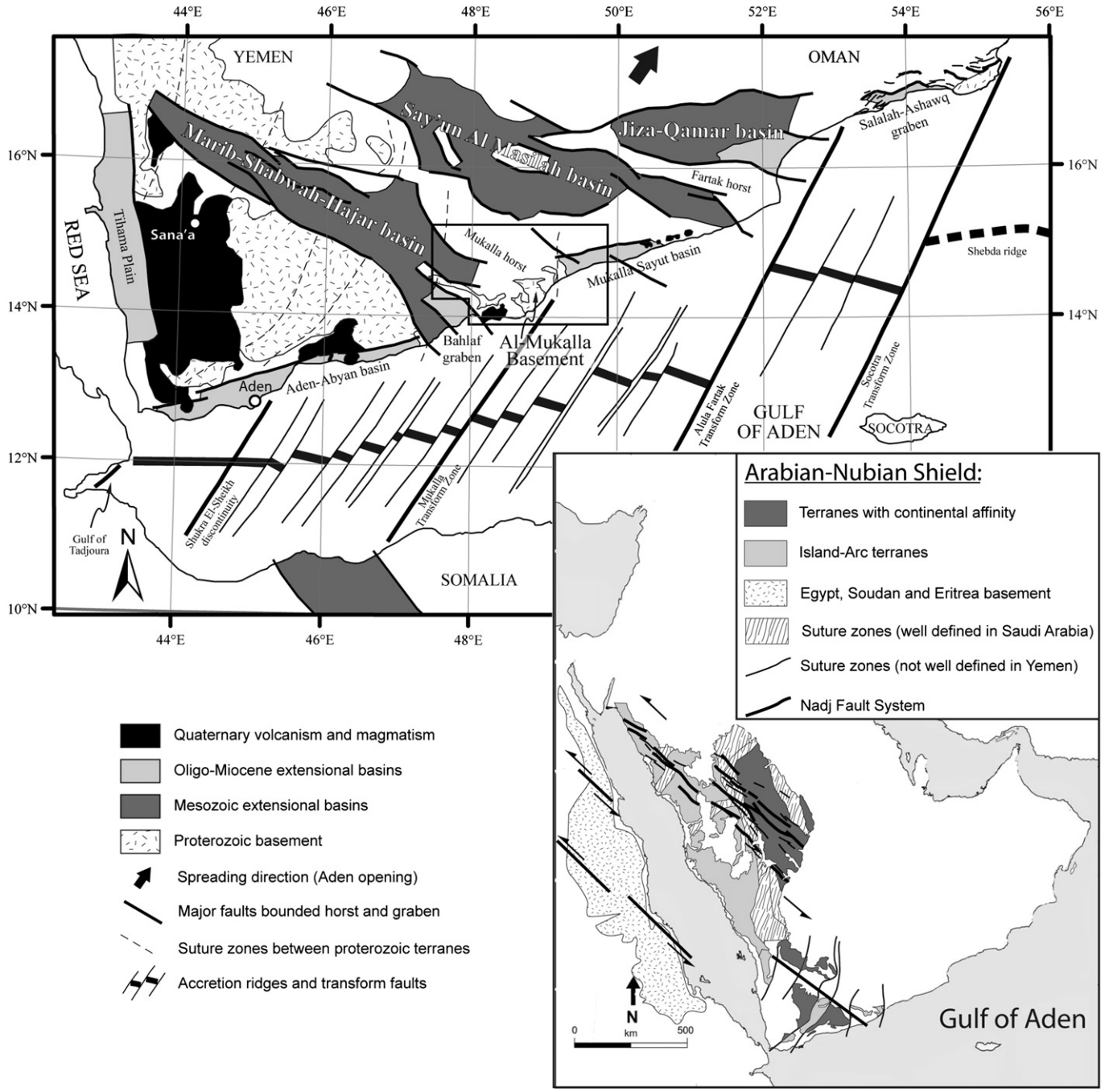

Fig. 1. Regional geological map of Mesozoic and Cenozoic basins of Yemen (based on GDR-surveying team and the Department of Geology & Mineral Exploration/Aden, 1987; Bosence, 1997; Lepvrier et al., 2002; Huchon and Khanbari, 2003). The black frame locates Fig. 2. The insert corresponds to a simplified map of the Yemenite and Arabian basement, with individualization of the main proterozoic terranes (based on Stoeser and Camp, 1985; Windley et al., 1996).

are predominantly dilational fractures (or type I fracture) even if minor shear component is sometimes observed. Areas of granite, where primary fractures prevail, correspond to the protolith (Caine et al., 1996). For the sake of clarity, we will use from now the term *joint* for describing *primary fractures*.

4.2. Secondary fractures and fault zone concept

It has become common in recent years to describe fault zones as comprising two components (Fig. 4d): a fault core and an associated damage zone (Chester et al., 1993; Caine et al., 1996). The fault core contains slip surfaces, gouge, cataclasites and breccias, and corresponds to the zone where most of the displacement is accommodated. Damage zone is generally taken as the volume of deformed wall rocks around a fault core that results from the initiation, propagation and build-up of slip along faults (Kim et al., 2004). Damage zone thickness corresponds to the zone within which fault and fracture density is higher than the background density (Childs et al., 2009).

This simple conceptual model for fault zone structure has been widely confirmed by field examples (e.g. Schulz and Evans, 1998; Micarelli et al., 2003; Géraud et al., 2006). In the Burum granite,

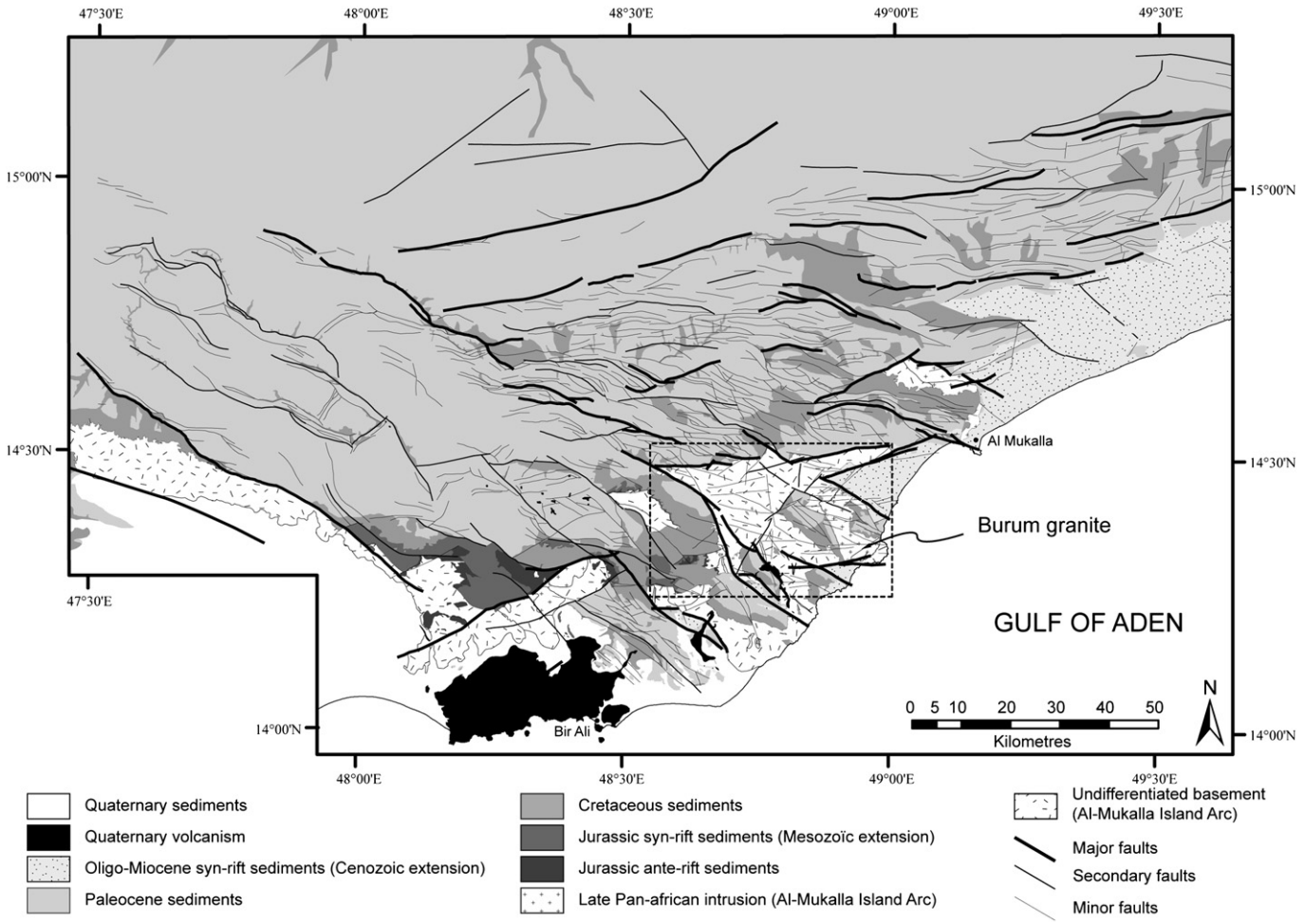

Fig. 2. Geological and structural map of the Mukalla horst modified from geological maps of Republic of Yemen (GDR-surveying team and the Department of Geology & Mineral Exploration/Aden, 1987). The map localization is indicated in Fig. 1. The dashed black frame locates Fig. 5a.

fault zones are in accordance with this general scheme and a typical example is presented in Fig. 3a. The main fault plane, located at the contact between fault core and the foot wall, is oriented N155°E with a SW dip direction of 85° and is associated with a 10 m thick core. The fault core consists of cataclasite cemented by calcite, crush-breccia and a fault gouge characterized by illitisation and kaolinization alteration. An important characteristic of this fault zone is the asymmetric distribution of damage zones, with an intensively deformed Damage Zone in the Hanging Wall (DZ-HW), and a weakly deformed Damage Zone in the Foot Wall (DZ-FW) (Fig. 3a). The DZ-FW is less than 20 m wide, with a moderately dense fracture density which decreases progressively toward the protolith. The DZ-FW is characterized by sub-vertical fractures which have strikes roughly parallel to the main fault plane. No breccias or gouge zone have been observed in the DZ-FW. The DZ-HW, up to 50 m wide, consists of highly fractured granite, with some localized crush-breccia characterized by illitisation and kaolinization. The fracture network is dense and well-organized. An orientation data diagram (Fig. 3a) shows a conjugated fracture pattern affecting the DZ-HW. Three main sets are recognized: one around N155°E, one around 140°E and one around N070°E. This fracture pattern is interpreted as R- and R′-shear surfaces of a Riedel system formed in a N155°E trending fault zone with a major sinistral component (Fig. 3a).

This model of fault zone is well-adapted for describing architecture and size (i.e. thickness) of a given fault at field scale. However, when attempting to understand multi-scale organization of fracturing, as proposed in this study, notion of scaling has to be considered when defining a fault zone. Indeed, a fault zone, as described above, contains in its damage zone several fault zones of low order which have their own fault core and damage zone (Fig. 4e). In the same way, this fault zone can be part of a fault zone of high order which contains a complex system of fault cores and damage zones which branch, anastomose and link, entraining blocks or lenses of relatively undeformed protolith (Fig. 4c) as proposed by recent researches (Faulkner et al., 2003; Géraud et al., 2010). An example of this complex system of fault cores and damage zones that characterized large fault zones, as proposed by Faulkner et al. (2003), has been observed on the field. Indeed, a succession of zones of high fracture intensity between relatively less fractured rocks is often observed in the vicinity of main fault zones like the one illustrated on Fig. 4d. We named these structures: fracture corridors (Figs. 3b and 4c). Zones of high fracture intensity correspond to both minor fault zones up to 1 m wide and clusters of shear fractures, while zones of low fracture intensity have the characteristics of the protolith with primary fractures network. The principal characteristic of these fracture corridors is the presence of sub-parallel and sub-vertical main fracture planes which delimit zones of high and low fracturing intensity (see stereogram in Fig. 3b). They can exceed 50–100 m in width and are considered as secondary structures mechanically related to the main fault zone.

Consequently, we will not use the fault zone definition of Caine et al. (1996) because is scale limited. We prefer used the definition

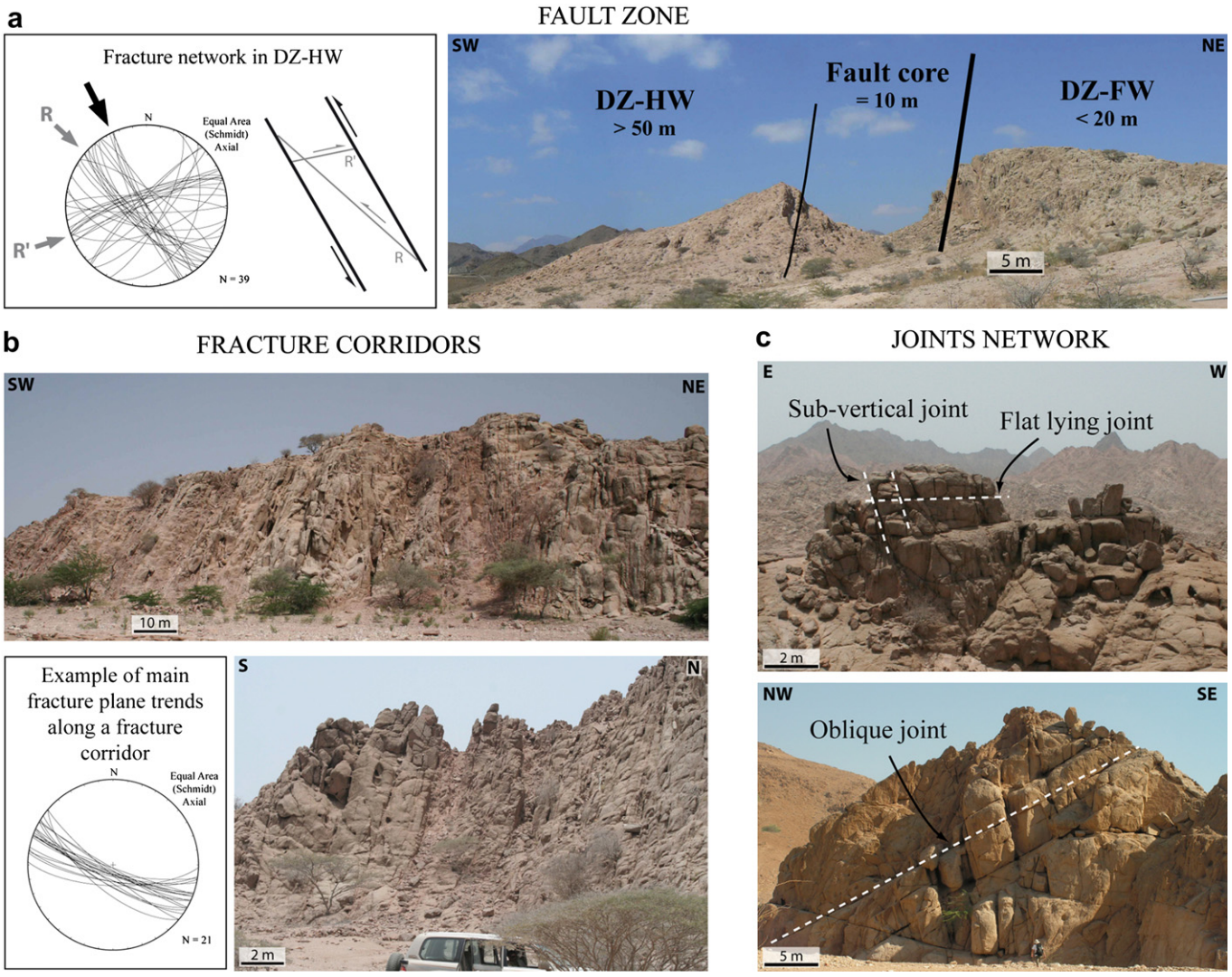

Fig. 3. Main structures highlighted in Burum granite: (a) major fault zone with a central fault core, an intensively deformed Damage Zone in the Hanging Wall (DZ-HW), and a weakly deformed Damage Zone in the Foot Wall (DZ-FW); (b) fracture corridors; (c) Joint network. Examples of fracture networks collected in the field are shown for the DZ-HW of the major fault zone and for the NW–SE trending fracture corridors.

of Peacock et al. (2000) which permits fault zones description at all scales of observation: a fault zone is a system of fault segments that interact and link and are restricted to a relatively narrow band or volume. In order to facilitate the classification of fault zones identifying from regional to field scale during this study, an order of magnitude will be attributing to each fault zone according to the scale of observation and consequently to its size (see Section 6.3).

5. Datasets of multi-scale fractures in the Mukalla basement

Four structural maps are used for the multi-scale statistical analysis of fracturing. Digitizing of ASTER satellite imageries (Fig. 5a) and interpretation of a Digital Elevation Model (DEM, SRTM 90 m) have been used to construct the Mukalla basement map (Fig. 6a) at a sampling scale of 1/40000. The Burum granite map at a sampling scale of 1/15000 (Fig. 6b) was constructed by digitizing and interpretation of high resolution QUICKBIRD satellite imageries (Fig. 5b). The structural lineament interpretation was completed by a geomorphological analysis which consists of tracing lineaments where wadis radically change their courses (Fig. 6b). Lineament mapping was focused on the northern part of the Burum granite (Fig. 5b). High resolution picking of structural lineaments has been carried out on high resolution QUICKBIRD imagery at a sampling scale of 1/1500 for constructing a detailed Burum granite map (Fig. 6c). This map was realized in the north-western part of the Burum granite where granite is well-preserved from weathering and erosion. 4738 lineaments were picked for a surface area of 10 km^2. Finally, a very accurate picking performed at the highest resolution on QUICKBIRD imagery (i.e. sampling scale of 1/500) was realized on a structural micro-block (Fig. 7). 2218 lineaments were picked in the micro-block for a surface area of 0.5 km^2.

6. Multi-scale statistical analysis of geometric parameters

6.1. Orientation analysis

Histograms of orientation, in which frequencies are weighted according to lineament length, have been realized for each map (Fig. 8). The weighted lineament method considers the strike of each segment which constitutes a lineament and generates a histogram from the cumulated length of all segments for each specific direction. This method seems to be the best suitable for this

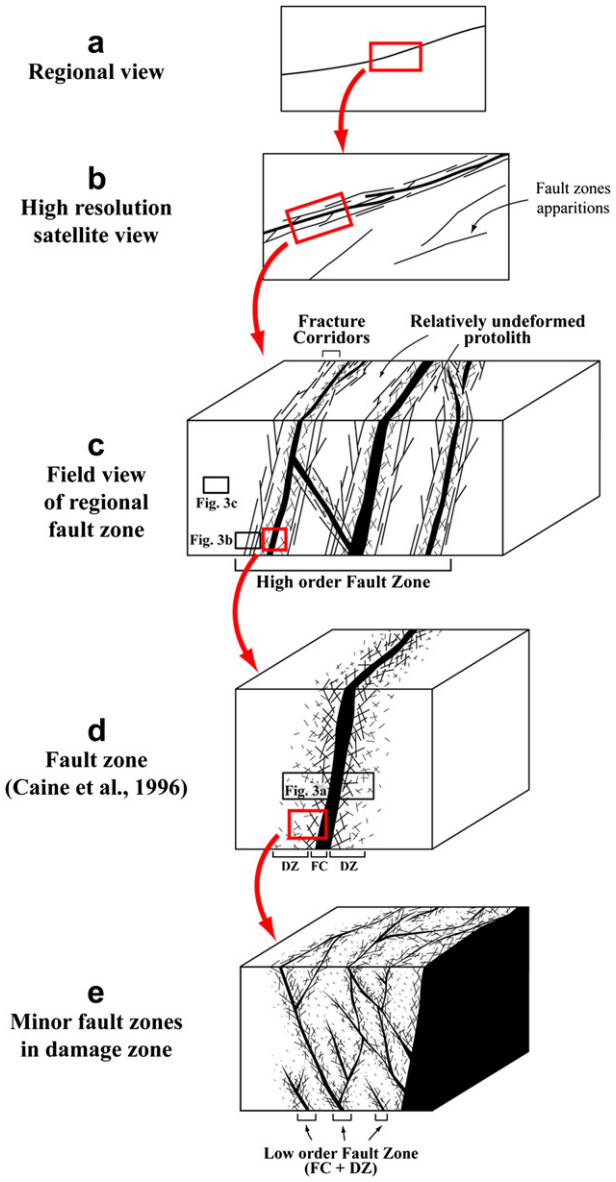

Fig. 4. Schematic representations of fault zones observed from regional to field scales, showing the relationships between fault zones of different orders of magnitude. (a) Regional fault zone represented by a single lineament when observed at satellite scale (map view). (b) When increasing the scale of observations, (i) internal structures of regional fault zone can be specified, and (ii) fault zones of low order are recognized (map view). (c) High order fault zone formed by several fault zones like in (d) separated by blocks or lenses of relatively undeformed protolith. Note the presence of fracture corridors at the interface between fault zones and protolith. (d) Typical fault zone structure with a fault core surrounding by damage zones (after Caine et al., 1996). (e) Low order fault zones constituting the damage zone of a fault zone like in (d). Analogies between field observations (Fig. 3) and fault zones models are indicated by the black frames. DZ: Damage Zone; FC: Fault Core.

kind of study since it considers frequency, length and curved shape of lineaments.

At the sampling scales of 1/40000 and 1/15000, histograms of orientation show three main orientation sets (Fig. 8). While first order peaks correspond to E–W and NW–SE structures, the second order peak corresponds to NE–SW structures. This orientation distribution is well-illustrated on Fig. 6a where structural network is mainly controlled by E–W and NW–SE lineaments, whereas NE–SW lineaments are localized along a single narrow band located in the centre of the map (Fig. 6a).

At larger scales (i.e. 1/1500 and 1/500), four peaks are observed: N–S, NE–SW, E–W and NW–SE (Fig. 8). First order peaks correspond to E–W and N–S structures. These orientation sets are characterized by narrow peaks lying in an interval of up to 10°. In contrast, second order peaks, which correspond to NE–SW and NW–SE structures, have more scattered azimuth distributions lying in an interval of up to 30° (Fig. 8).

All orientation sets observed at the regional scales (i.e. 1/40000 and 1/15000) are present at larger scales (i.e. 1/1500 and 1/500). On the other hand, the occurrence of a new orientation set, trending N–S, is observed at larger scales where minor structures are visible (i.e. minor faults, fracture corridors and joints).

For a given orientation set, the mean frequency peaks appear to vary only slightly from one scale to the next (Fig. 8). However, it is interesting to note that E–W and NW–SE orientation sets have the same azimuth properties (i.e. proportion and degree of scattering) at scales of 1/40000 and 1/15000, while at larger scales the frequency of the NW–SE set decreases and the azimuth scattering decreases for the E–W set. This means that these fracture sets can have different geometric properties at large scale even if they display the same behavior at smaller scale. This feature reveals differences in the mechanism of formation for these two orientation sets, and this will be discussed later in this paper.

6.2. Length analysis (2D)

Statistical analyses concerning the fracture-length distributions have been performed using the 2D datasets (i.e. maps presented in Figs. 6 and 7). Length distributions are characterized using log–log diagram where the cumulative frequency distribution $N(l)$ (number of fractures with length greater or equal to length l) is plot versus the length l (Fig. 8). When comparing fracture-length distributions plot for different scales, a normalized cumulative frequency distribution is used, where $N(l)$ corresponds to the number of fractures with length greater or equal to length l divided by the surface of the studied map (Fig. 9). These cumulative frequency distributions of length can be described by several theoretical laws. Exponential, log-normal and power-law distributions are the most common models used to describe the fracture-length statistics (Bonnet et al., 2001). From the study of natural fractures datasets, Castaing et al. (1996) and Odling et al. (1999) among others show that fault length distributions often follow a power-law relation such as $N(l) = \alpha l^{-a}$, where α is a constant characteristic of the scale, and a is the power-law exponent generally ranging between 1 and 3 (Bour and Davy, 1997; Odling, 1997). The power-law exponent characterizes the relative abundance of fractures of different sizes. A fracture-length distribution exhibiting power-law behavior means that length distribution is scale-invariant over the spatial range considered. When logarithmic axes are used, a straight line indicates that the length distribution is power-law with a slope defined by the exponent a. In most cases, sampling effects at small and large scales may cause a deviation of the experimental log–log plot from a theoretical perfect straight line. The sampling biases are named as “truncation” and “censoring” (Pickering et al., 1995; Bonnet et al., 2001), and correspond respectively to (i) an underestimation of the small fractures due to the spatial resolution limitations of the sampling method used and (ii) to an underestimation of trace lengths for fractures greater than the sampling area dimensions or that intersect the sampling area boundary.

Fig. 9 compares the cumulative length distributions of fractures observed in the four structural maps presented in section 5 (Figs. 6 and 7). Such plots have been extensively presented in the literature on the scaling of fracture-length distributions (Castaing et al., 1996; Odling, 1997; Odling et al., 1999). The majority of these maps shows trace-length distributions close to negative exponential laws. The Burum granite map at the scale of 1/1500 is the only dataset that

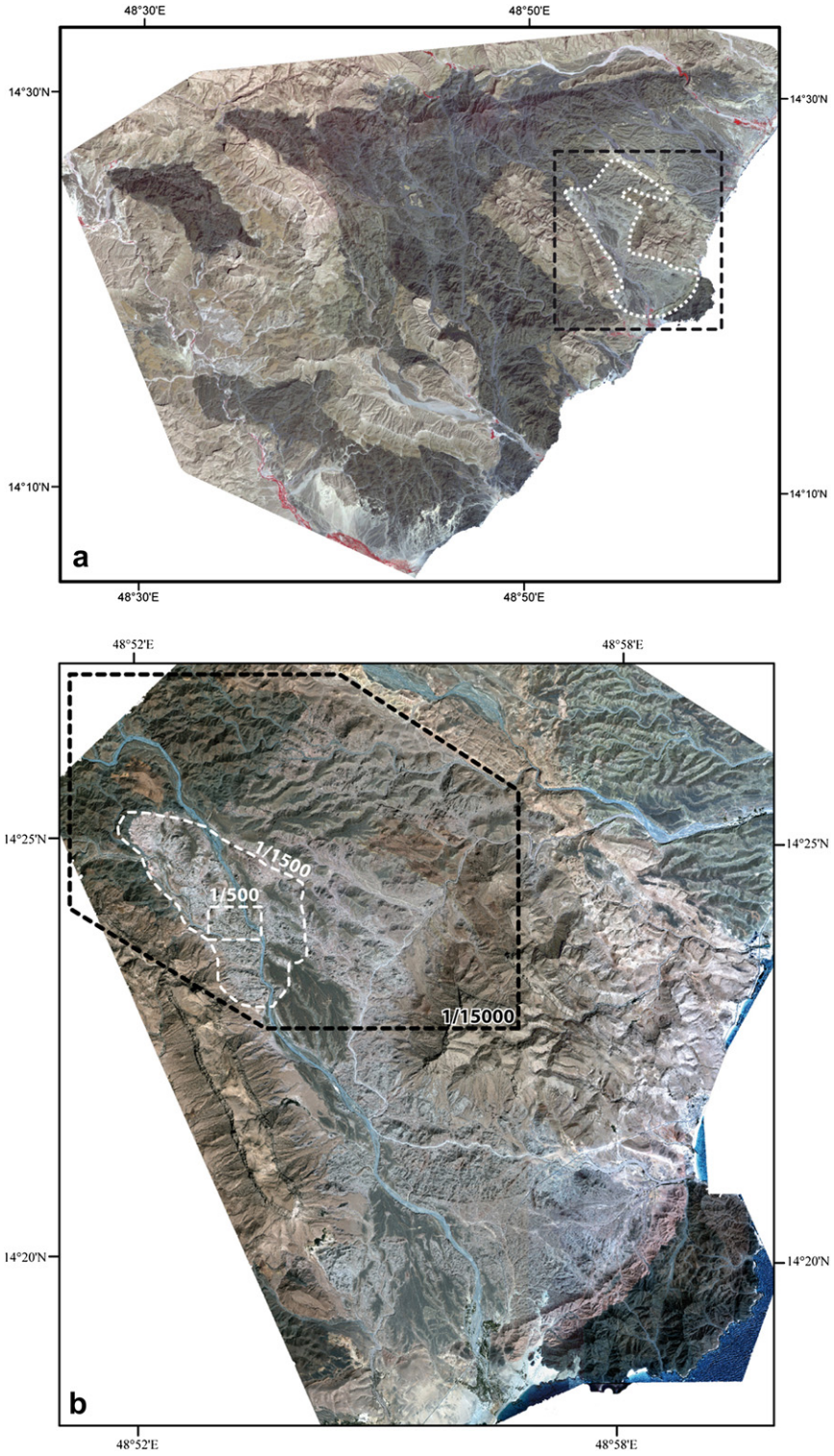

Fig. 5. (a) Aster images of the Mukalla basement. The dashed white frame locates Burum granite and the dashed black frame locates Fig. 5b. (b) Quickbird satellite view of Burum granite. Dashed frames locate maps of Figs. 6b, c, and 7.

exhibits a well-defined power-law length distribution over a scale range of 100–1000 m, and characterized by an exponent equal to 1.8 (Fig. 9). However, when considering the length distributions of the overall maps, the log–log plot reveals overlapping curves, whose general envelope is a straight line characterized by a slope of 1.8 (Fig. 9). This suggests the presence of an underlying power-law distribution of the fracture trace-length within the Mukalla basement over 3 orders of magnitude (10–10000 m), as already proposed by several previous authors for basement studies (Castaing et al., 1996; Odling, 1997). Correspondence between the slope values for the Burum granite map at scale of 1/1500 and the underlying power-law confirms the validity of this power-law. The

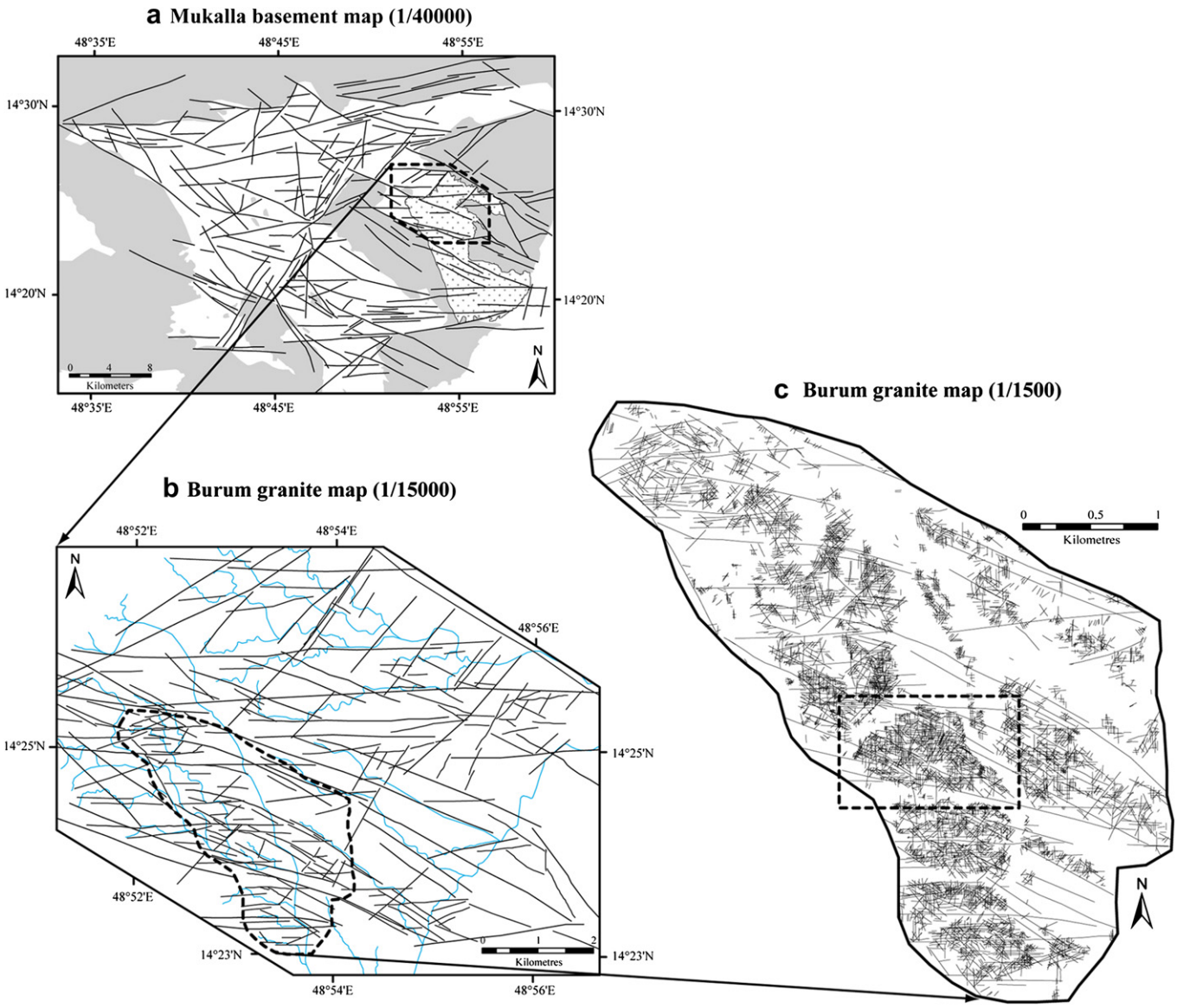

Fig. 6. Structural maps at different scales of the Mukalla proterozoic basement. (a) Mukalla basement structural map at a sampling scale of 1/40000. Mesozoic and Cenozoic cover is represented in grey and the Burum granite with crosses. The dashed black frame locates Fig. 6b. (b) Burum granite structural map at a sampling scale of 1/15000. Wadis are represented in blue. The dashed black frame locates Fig. 6c. (c) Burum granite map at the sampling scale of 1/1500. Dashed black frame locates Fig. 7. (For interpretation of the references to colour in this figure legend, the reader is referred to the web version of this article.)

apparent negative exponential distributions laws observed for each individual map curves are therefore not relevant and probably represent truncation and censoring effects, while the well-defined power-law distribution observed for the Burum granite map at the scale of 1/1500 can be explained by the larger surface area used that reduced censoring effects.

The trace-length distributions just presented above have been realized using the whole datasets whatever the fracture orientations. To try to visualize the effect of the orientation parameter on the fracture-length distribution, the main orientation sets were studied separately. The micro-block map was chosen to perform this detailed study because all the individual structures are represented at this scale (i.e. faults, fracture corridors and joints). Orientation sets were chosen according to the mean peaks previously identified in the orientation histograms (Fig. 8), i.e. N–S (N170-010°E), NE–SW (N030-050°E), E–W (N080-100°E) and NW–SE (N110-130°E). The global distribution, including all orientation sets, is represented by a regular curve (Fig. 9) which closely matches with a negative exponential distribution. When regarding to individual orientation sets, two different length distributions can be distinguished (Fig. 10). E–W and NW–SE orientation sets show length distributions which approximate a power-law over a scale range of 20–100 m, with an exponent of 1.7 (Fig. 10a and b). By contrast, the N–S and NE–SW orientation sets are best described by a negative exponential relationship (Fig. 10c and d). The fact that orientation sets which are sub-parallel to bounding faults of the micro-block (i.e. E–W and NW–SE) show power-law length distributions reveals that tectonic systems seem to be scale-invariant. On the contrary, fracture sets which are not related to faults (i.e. N–S and NE–SW) show negative exponential length distributions. Negative exponential shapes of N–S and NE–SW length distributions are not due to truncation or censoring, because these laws are perfectly well-defined in an interval between the upper cutoff (100 m) and the lower cutoff (20 m) of the power-laws length distributions of E–W and NW–SE trending families (Fig. 10).

This difference of length distribution behavior for fault related and non-fault related fracture systems is emphasized by the study of the

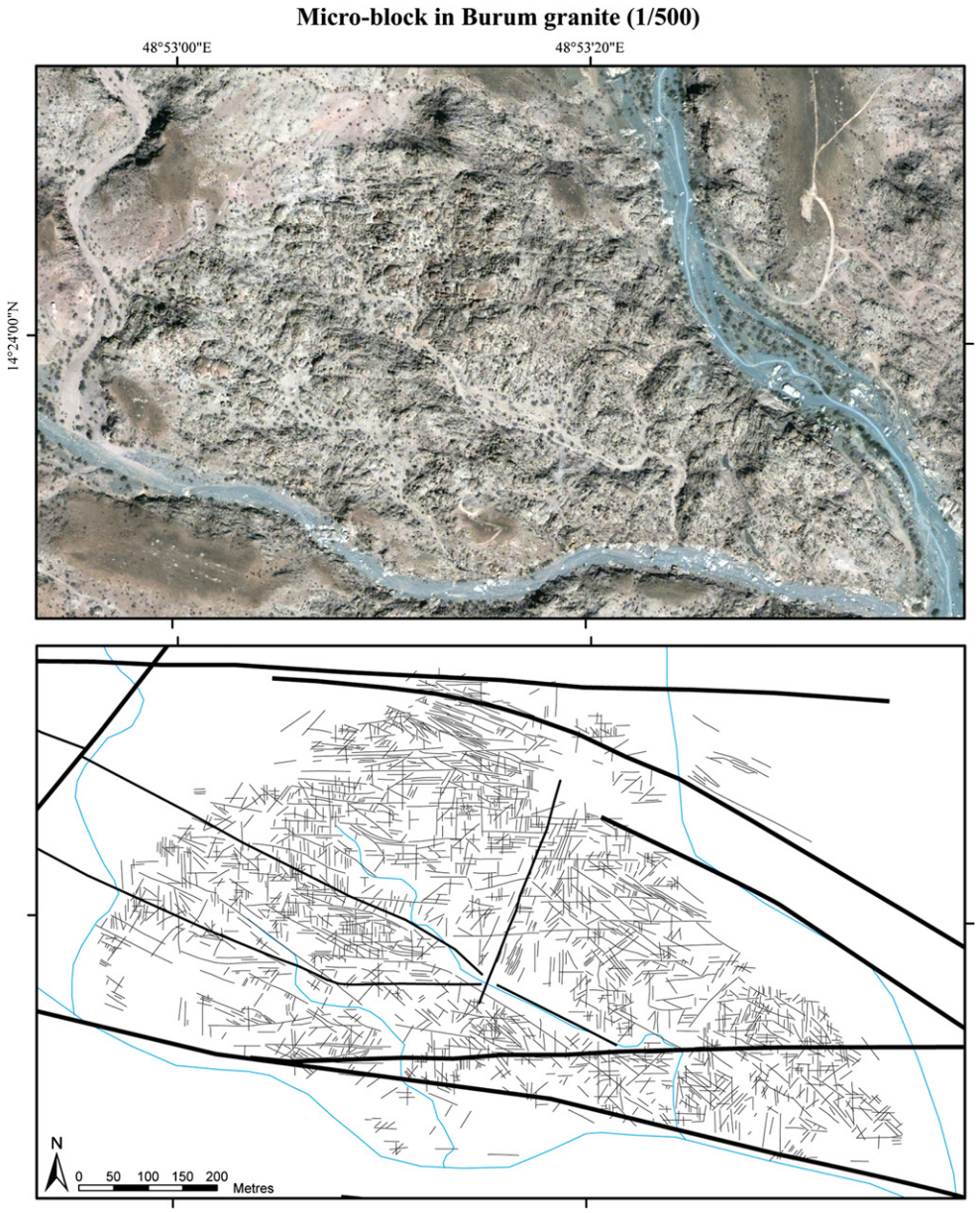

Fig. 7. Map of structural micro-block in Burum granite at the sampling scale of 1/500. Wadis are represented in blue, major fault zones in thick black lines, and minor fractures in thin black lines. (For interpretation of the references to colour in this figure legend, the reader is referred to the web version of this article.)

orientation distributions calculated with the identification of several classes of length for the larger scale (Fig. 11). Four ranges of lengths have been separated: trace lengths lower than 25 m, from 25 to 50 m, from 50 to 100 m and trace lengths higher than 100 m. This segregation shows clearly lower frequencies for the N–S and NE–SW trending fractures in the classes of highest lengths. In a same time, the frequencies of the E–W and NW–SE trending fractures show increasing values when length lineaments are longer than 50 m. This means that the datasets that show negative exponential length distributions are characterized by the presence of small fractures that are therefore restricted to a characteristic scale range (i.e. <50m).

6.3. Spatial distribution analysis

Two types of spatial distribution of fractures are analyzed in this section: (i) some major fault zones network and (ii) some micro-block fracture systems.

6.3.1. Major fault zones network and multi-scale structural blocks

As explained in Section 4, fault zones can be determined upon several orders of magnitude, from regional to field scales (Fig. 4). Maps constructed at regional scale (i.e. 1/40000 and 1/15000) will enable us to identify these different orders of magnitude of fault zones in considering the scale of observation and the length of the structural lineaments. Firstly, when increasing the scale of observation (i.e. from scale of 1/40000 to scale of 1/15000), fault zones of low order become visible, and consequently are distinguished (i) those contributing to internal architecture of high order fault zone and (ii) those individualizing low order structural blocks (Fig. 4a and b). Secondly, as reported by numerous studies which have highlighted the scaling relationships between fault length and fault displacement (Clark and Cox, 1996; Schlische et al., 1996; Schultz et al., 2008), refinement of maps according to lineaments length will be performed for recognizing the limits and the dimensions of multi-scale structural blocks.

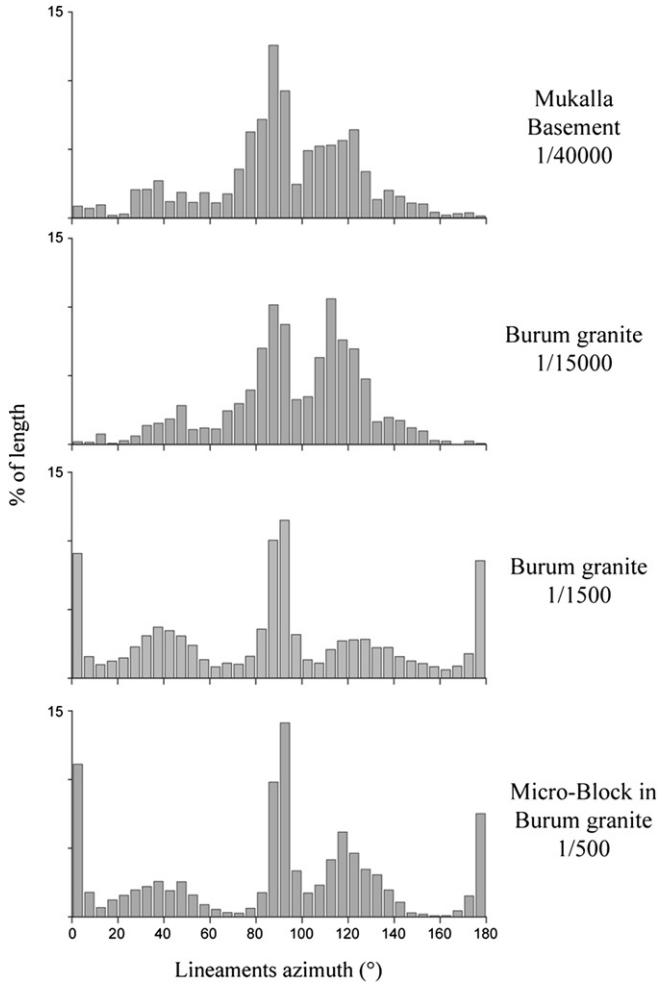

Fig. 8. Histograms of fracture orientation at each scale of sampling. Note the extremely regular azimuth distributions of E–W and N–S sets at sampling scales of 1/1500 and 1/500, which are included in an interval up to 10° (see text for more explanations).

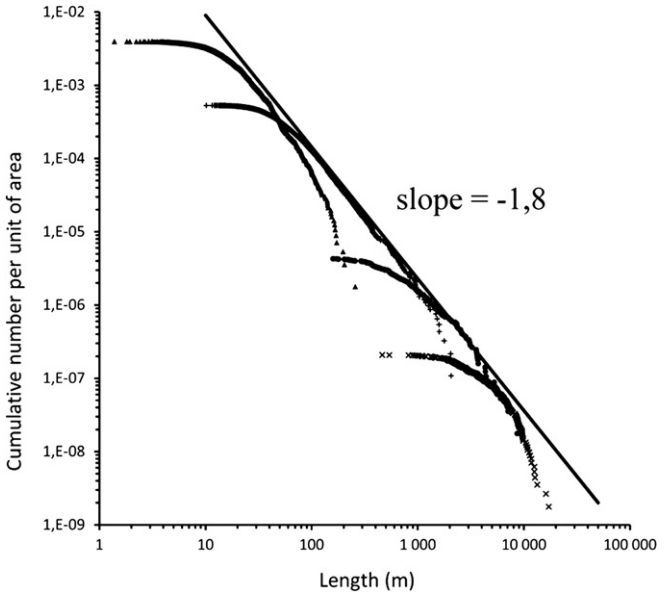

Fig. 9. Normalized cumulative frequency distributions, $N(l)$, for fracture lengths, l, from maps ranging from regional to micro-block scales (i.e.× 1/40000, ● 1/15000, + 1/1500, and ▲ 1/500). Individually, datasets show in majority negative exponential length distributions but collectively they show overall power-law behavior. Note the well-defined power-law for the Burum granite map at sampling scale of 1/1500.

Spatial and hierarchical organizations of the two main orientation sets of fault zones, i.e. E–W and NW–SE, have been investigated individually (Figs. 12 and 13). For each orientation set, refinement of datasets has been performed on the Mukalla basement map (Fig. 6a) and the Burum granite map (Fig. 6b) according to lineaments length. From the Mukalla basement map, three refined maps have been realized: lineaments >9 km (Figs. 12a and 13a), lineaments >5 km (Figs. 12b and 13b), and complete dataset (Figs. 12c and 13c). From the Burum granite map, three refined maps have been realized: lineaments >3 km (Figs. 12d and 13d), lineaments >800 m (Figs. 12e and 13e), and complete dataset (Figs. 12f and 13f).

Fig. 12a shows that long lineaments are localized into two main fault zones spaced by 17–20 km (FZ1 and FZ2). Two other long lineaments (FZ3) are intercalated between these two deformation zones that individualized structural blocks 10 km in width. When lineaments 5–9 km long are added (Fig. 12b), intermediate structural blocks appear and are characterized by widths from 3 to 5 km. In addition, internal structures of FZ1, FZ2 and FZ3 can be estimated. FZ1 and FZ2 present clusters of fault zones with a large range of length and are characterized by thicknesses close to 4 km (Fig. 12b and c), while FZ3 thickness can be estimated of 2 km.

According to the interpretation of the Mukalla basement map made previously (Fig. 12c), the Burum granite map is cross cut by FZ3. At this scale of observation, FZ3 is composed of several fault zones with a large range of length (Fig. 12f) and has a thickness close to 2 km, as previously estimated. Fig. 12d shows that, south of FZ3, lineaments up to 3 km delimit structural blocks 1.5–3 km in width. When lineaments up to 800 m are represented, structural blocks 1.5–3 km in width are divided into several micro-blocks 700–900 m in width (Fig. 12e).

In the light of these observations, the E–W tectonic set shows hierarchical spatial distribution of fault zones, where fault zones are almost regularly spaced when looking between two fault zones of higher order (Fig. 12). Three main orders of block size have been defined thanks to scale of observation: pluri-kilometric or first order block sizes (Fig. 12a), kilometric or second order block sizes (Fig. 12b and d) and pluri-hectometric or third order block sizes (Fig. 12e).

Multi-scale analysis realized for NW–SE trending fault zones presents hierarchical distribution and spacings values close to E–W one (Fig. 13). However, regular spacings of fault zones are less obvious because (i) the Burum granite map at a scale of 1/15000 is located in a linking zone of several first order fault zones (Fig. 13c) and (ii) NW–SE trending structures are inherited from the Pan-African orogeny that can disturb spatial organization of fault zones. Consequently, the model of hierarchical distribution of fault zones presented below will be constructed from E–W trending fault zones results (Fig. 12).

6.3.2. Micro-block fracture systems

The micro-block map (Fig. 7), which allows mapping of minor fault zones, fracture corridors and joints, has been used for describing the spatial distribution of fractures within a third order block size (Fig. 12f). The micro-block map is particularly well-adapted because: (i) well-preserved outcrops allow a very exhaustive mapping and enable us to propose a realistic model for the spatial distribution of structural objects and (ii) it is bounded by E–W and NW–SE trending fault zones (Fig. 7) making it representative of the whole Burum granite with its typical parallelogram shape.

Lineaments datasets (Fig. 7) were used to construct density maps (Fig. 14) which were generated with the SIGEOL® software using an algorithm which computes the cumulated length/unit of

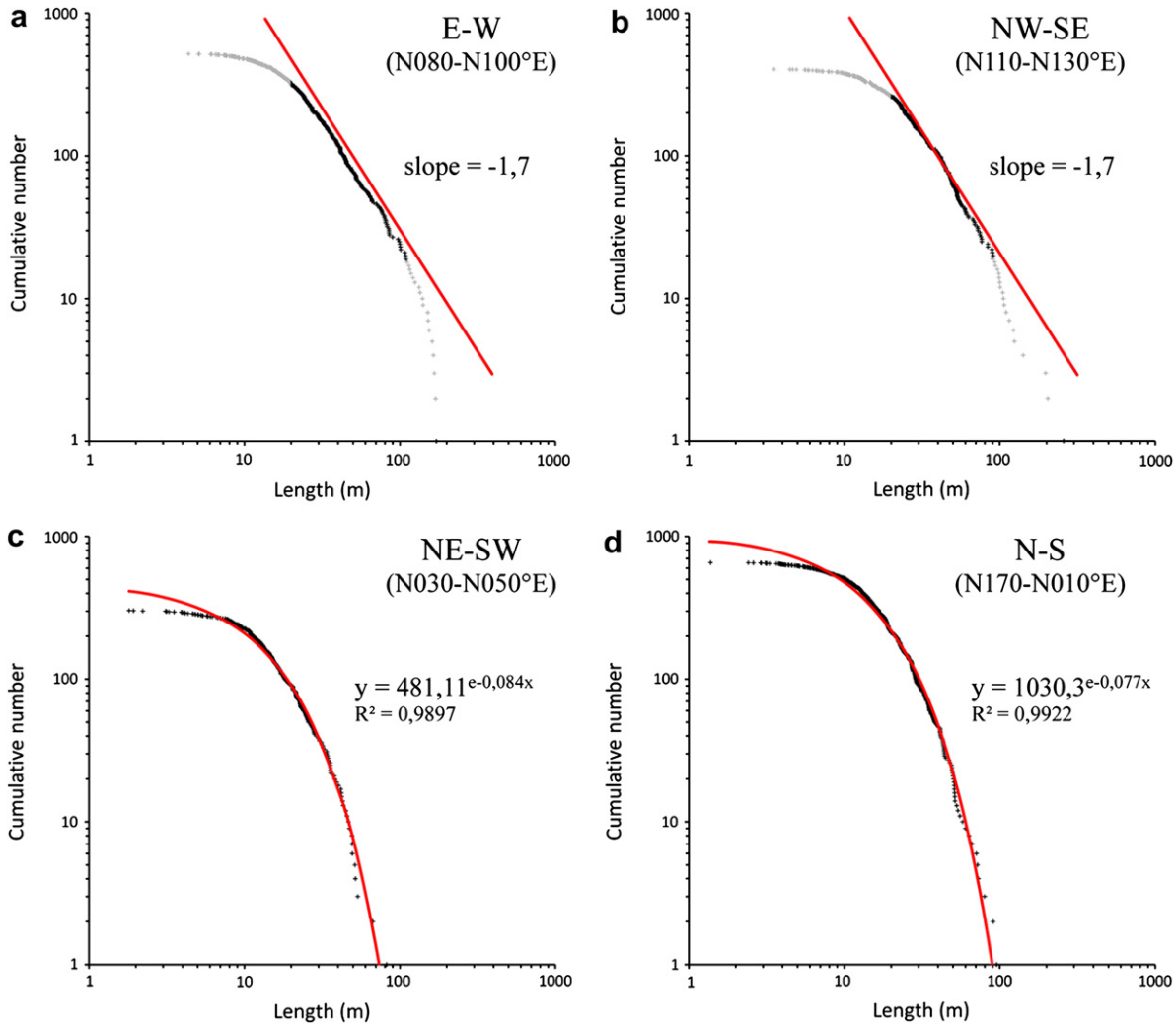

Fig. 10. Cumulative frequency distributions, *N(l)*, for fracture lengths, *l*, at micro-block scale (i.e. 1/500). The dataset has been refined in order to analyze each main orientation set: N–S (N170-010°E), NE–SW (N030-050°E), E–W (N080-100°E) and NW–SE (N110-130°E). E–W and NW–SE orientation sets show length distributions which approximate a power-law (red lines) over a scale range of 20–120 m, with an exponent of 1.7. Data in grey are affected by censoring and truncation. N–S and NE–SW orientation sets are best described by a negative exponential relationship (red curves). (For interpretation of the references to colour in this figure legend, the reader is referred to the web version of this article.)

surface in a floating kernel of 20 m by 20 m. As a result, each pixel of the raster has the same size as the kernel and its value equates to the cumulative length in meter of all lineaments in the determined kernel. The output data is an 8-bit raster that is converted to vector using a weighted linear contouring method. Four maps were constructed according to the four main orientation sets: N–S (N170-N010°E), NE–SW (N030-N050°E), E–W (N080-N100°E), and NW–SE (N110-130°E) (Fig. 14).

Density maps for the N–S and NE–SW lineament families show homogenous densities, even if several zones with density higher than 800 m/hm^2 are present (Fig. 14c and d). These lineaments are not directly related to fault zones and, in particular, are less represented in the northern part of the micro-block, where E–W and NW–SE trending fault zones intersect. In addition, the density maps clearly show a greater fracture density for the N–S dataset.

The E–W and NW–SE families of lineaments present very different distributions compared to the two previous maps. Zones of very high density (>1280 m/hm^2) are often prominent, are linear shaped, and are intimately related to the boundary fault zones (Fig. 14a and b). The density map of E–W trending lineaments presents one major high density zone (A in Fig. 14a) which is related to the E–W trending fault zone at the northern boundary of micro-block. Another zone of high density is observed on the south-west part of the micro-block (B in Fig. 14a), and can be related to another E–W trending fault zone. When looking at the NW–SE trending lineaments, the density map shows one major zone of high density at the intersection between the E–W and NW–SE trending fault zones (C in Fig. 14b), and a small one in the eastern part of the micro-block (D in Fig. 14b). These two zones of high density are probably related to the same fault system trending NW–SE. In addition, the E–W trending lineaments seem to have a diffuse spatial distribution in the micro-block while the NW–SE ones are missing in the central zone of the micro-block.

Finally, all these density map analyses reveal that the orientation sets close to the trends of the bounding faults (i.e. E–W and NW–SE) show clustered spacing. On the contrary, the orientation sets oblique to bounding fault zones (i.e. N–S and NE–SW) show anti-clustered spacing, which is in accordance with field observations (see Section 4). In addition, density maps indicate: (i) the close relationship between clustering zones and the third order fault zones, and (ii) clustering zones close to 100 m wide.

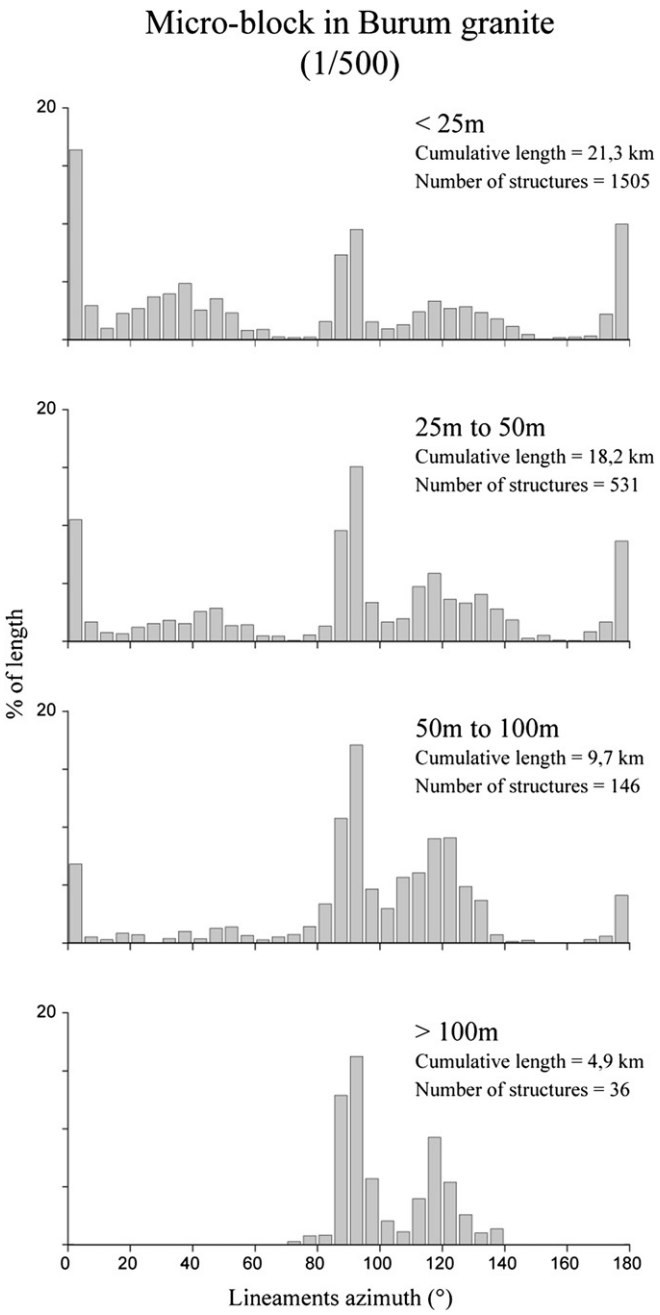

Fig. 11. Histograms of orientation according to families of length for the structural micro-block of Fig. 7 (<25 m, 25–50 m, 50–100 m and >100 m).

7. Model of fracture network and tectonic control

7.1. Hierarchical organization of fault zones and tectonic interpretation

The E–W and NW–SE fault zones show a hierarchical spatial distribution (Fig. 15a). Three orders of fault zone and block size dimensions have been defined: (i) first order fault zones > 20 km in length delimit blocks 10–20 km wide, (ii) second order fault zones 5–20 km in length delimit intermediate blocks 2–5 km wide, and (iii) third order fault zones 1–3 km in length delimit micro-blocks 700–1000 m wide. This geometry of the fault zones network corresponds to an interlocking of parallelogram shaped structural blocks of different order, where fault zones are almost regularly spaced when looking between two fault zones of higher order (Fig. 15a).

The fault zones thicknesses seem to be another attribute which is dependent on the fault zone dimension as well as their length and spacing. First order fault zones show thicknesses of 4 and 2 km (Figs. 12c and 15a), while thicknesses of second order fault zones are more difficult to precisely identify but can be estimated to be around 300–400 m (Figs. 12f and 15a). In the light of field observations and satellite interpretations, thicknesses of third order fault zones can be estimated to be around 150 m. Their principal characteristics are a central main fault zones surrounding by mechanically related secondary structures. These two end-members are assumed to be similar to fault zone (Fig. 3a) and fracture corridors (Fig. 3b) identified in the field (Fig. 15b and c). Their principal characteristics are: (i) a central fault core up to 10 m wide, (ii) an asymmetrical fault zone characterized by an intensively fractured damage zone in the hanging wall up to 50 m wide, and a weakly fractured damage zone in the foot wall up to 20 m wide, and (iii) a large zone of fault dampening, up to 100 m wide, composed of fracture corridors (see Section 4 and Fig. 3b for more details). The detailed analysis of the structural micro-block, where density maps point out the vicinity of fractures clusters and bounding fault zones (Fig. 14), confirms this geometry of third order fault zone described in the field.

The model of hierarchical distribution of fault zones proposed in this study (Fig. 15a) shows a “self-similar” geometry type as defined by Mandelbrot (1972), for length, spacing and thickness parameters. This means that the visualization of objects at all scales are indistinguishable. “Self similarity” can also be described as a fractal geometry, which is characterized by power-law distribution of the geometrical parameters such as length, spacing, or thickness (Gillespie et al., 1993; Castaing et al., 1996; Odling et al., 1999; Bonnet et al., 2001). In this study, the power-law length distributions have been observed in the case of the tectonic systems (Fig. 10). On the other hand, the power-law spacing distributions have not been described directly by statistical analysis. However, the notion of clustered spacings, that characterizes fractal systems, has been described in the Burum granite (see Section 6.3 and Fig. 14), and is ultimately contained in the relative thicknesses of fault zones of each order. Consequently, we can conclude that the E–W and NW–SE tectonic systems reveal a “self-similar” behavior.

The E–W and NW–SE conjugated sets correspond to the regional trends related to the Jurassic and Cretaceous rifting observed in this area (Bosence, 1997), where the NW–SE trend is inherited from the Pan-African orogeny (Redfern and Jones, 1995; Birse et al., 1997). These structures have been active during Mesozoic rifting mainly as normal faults. We can note that the NW–SE trending structures were reactivated during the Gulf of Aden opening (Khanbari, 2000; Huchon and Khanbari, 2003; Bellahsen et al., 2006) and this is highlighted by cartographic evidences: (i) continuity of the NW–SE trending faults in the Paleocene cover (Fig. 2), and (ii) geometry of the two minor Cenozoic extensive basins showing some particular triangular shapes (Fig. 2).

The NE–SW regional trend has a different spatial distribution, and is localized along a single major crustal deformation zone (Fig. 6a). The NE–SW fault set is interpreted as Cenozoic strike-slip faults corresponding to the onshore continuity of the Mukalla transform fault (Fig. 1).

7.2. Model of fracture network for third order block size

Protolith located between fault zones have been widely considered to be not affected by relevant deformation. However, the deformation inside third order blocks has to be taken into

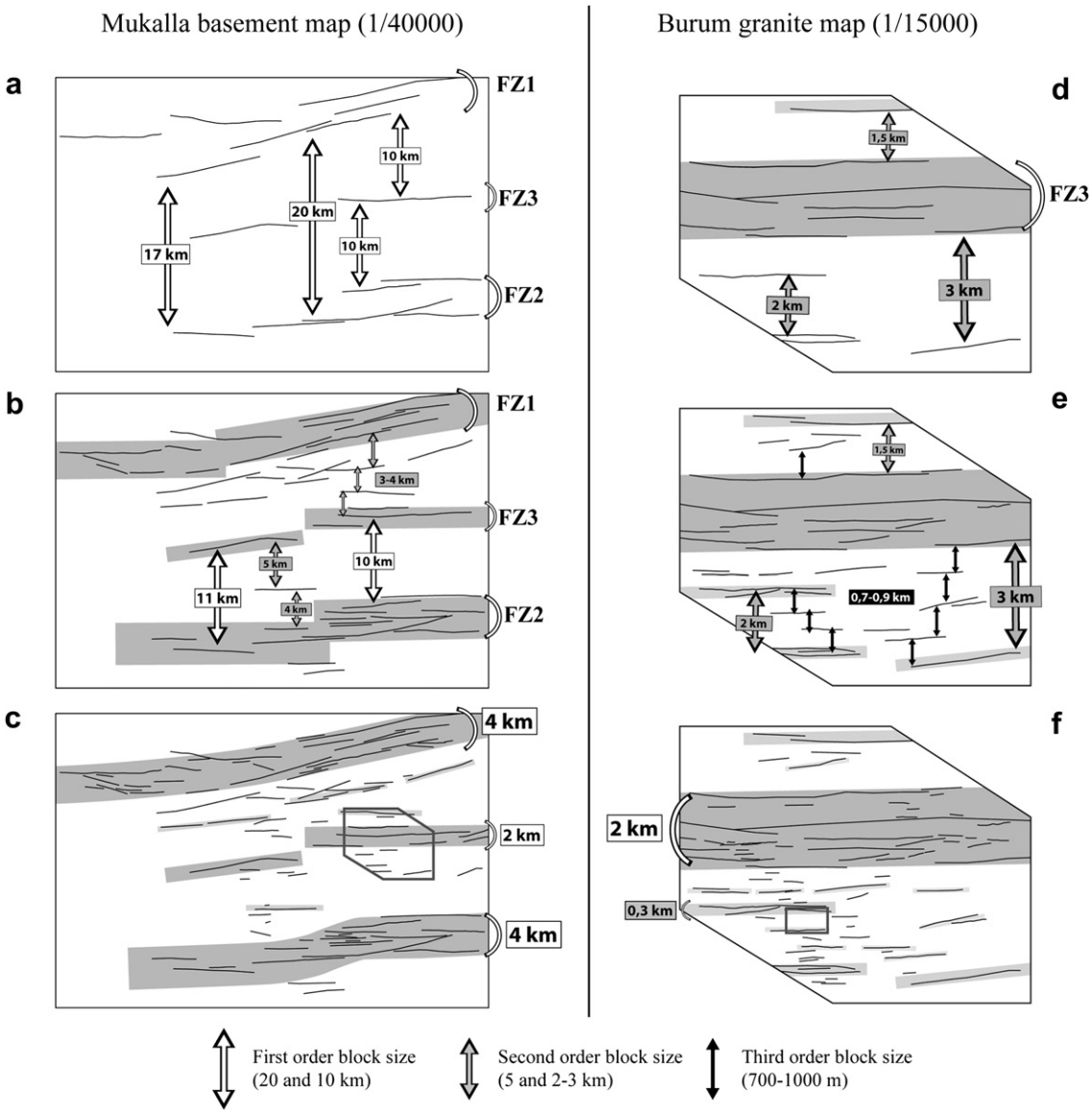

Fig. 12. Refined maps from the Mukalla basement map (Fig. 6a) and the Burum granite map (Fig. 6b) for E–W trending lineaments. From the Mukalla basement map, three refined maps have been realized: (a) lineaments > 9 km, (b) lineaments > 5 km, and (c) complete dataset. From the Burum granite map, three refined maps have been realized: (d) lineaments > 3 km, (e) lineaments > 800 m, and (f) complete dataset. Grey bands highlight main fault zones, brackets highlight thicknesses of fault zones of first and second orders, and black frames locate the Burum granite map and the micro-block map.

consideration when trying to quantify deformation or characterize the potential of fluid flow in such fractured reservoirs.

As described in the previous section, third order fault zones exhibit large zones of deformation around main fault zone, comprising a complex of fracture corridors interpreted as an area of fault dampening (Fig. 15b and c). When moving toward the central part of the micro-block, the fracture density decreases and the spatial distribution of fractures shows anti-clustered behavior (Figs. 7, 14 and 15b). E–W and N–S are the most prominent fracture sets in the central part of the micro-block (Fig. 14), while the NW–SE and NE–SW sets are poorly represented. The N–S orientation set shows several features which are typical of joint systems: (i) anti-clustered spacing (Fig. 14d), (ii) narrow orientation peaks lying in an interval of up to 10° (Fig. 8), (iii) negative exponential trace-length distribution characterized by the presence of small fractures (i.e. <50m) (Fig. 10d), and (iiii) hardly any N–S trending fault zone have been observed from the regional to the micro-block scales. The NE–SW structures also show at large scale evidence of a joint system with both negative exponential trace-length distribution (Fig. 10c) and anti-clustered spacing (Fig. 14c). This orientation set has a clearly lower density than the N–S trending fractures, and is interpreted as a minor joint set.

The E–W and NW–SE orientation sets show different behaviors when examined in the central part of the micro-block: (i) the E–W trending structures are more frequent than the NW–SE trending structures, which are only localized near bounding fault zones (Figs. 7 and 14), and (ii) the E–W orientation set show a narrower peak which lying in an interval up to 10° as already identified for the N–S orientation set (Fig. 8). Therefore, the N–S and E–W fracture sets have same spatial distribution and density values in the central part of the micro-block (Fig. 14), and both of them show an extremely homogenous azimuth distribution (Fig. 8). These features plus the high angle between the orientations of these two fracture sets allow us to interpret it as a typical orthogonal joint system, probably formed during granite cooling as “primary fractures” (Price and Cosgrove,

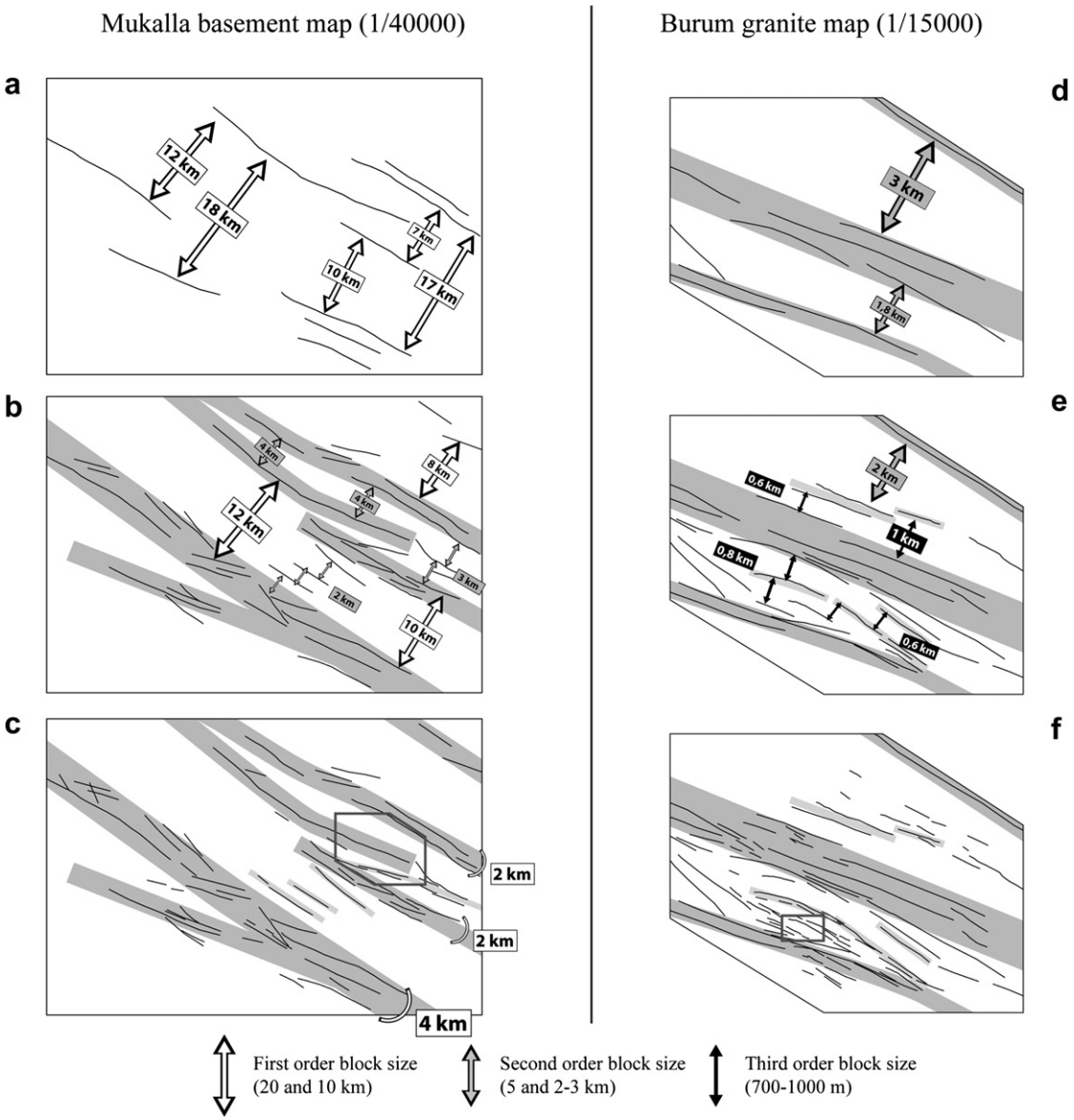

Fig. 13. Refined maps from the Mukalla basement map (Fig. 6a) and the Burum granite map (Fig. 6b) for NW–SE trending lineaments. See legend of Fig. 12 for more details.

1990; McCaffrey et al., 2003). Inspection of the central part of the micro-block in Fig. 7 reveals that the E–W trending fractures are longer than the N–S ones and that the N–S fractures are systematically cutoff by the E–W ones. These features are interpreted as reactivation of the E–W joint set during Mesozoic rifting (Fig. 15b).

Finally, the central part of the micro-block is characterized by an orthogonal joint system composed of N–S and E–W trending joints, and by a minor NE–SW trending joint set. The E–W set has a specific geometry because the initial short E–W joints have been reactivated and consequently have formed long structures by coalescence (Fig. 15b). At this scale, where joint systems are distinguishable, the fracture network does not show "self-similar" behavior or fractal geometry.

8. Fractured reservoir properties and fluid flow implications

8.1. Applications for fractured reservoir characterization

The model of fracture network established in this study provides major constraints on geologic properties important for site suitability, such as fracture network scaling, connectivity or structural blocks sizes. For instance, the well-organized fault zone network described from pluri-kilometric to pluri-hectometric scales is a model that can be used for defining the general framework of the reservoir or predicting localization and geometry of fault zones. Characteristics of lengths, spacings, and thicknesses of fault zones will be important geologic features for interpreting well data. In addition, this fault zone network can then be exported to reservoir simulation codes for comparison with production data or well tests.

We have determined that tectonic systems, in the proterozoic basement of Yemen, are characterized by a power-law trace-length distribution. This scale-invariant character has been previously described by numerous authors for a variety of fracture systems (see Bonnet et al., 2001 for a review). However, originality of this work is the consistency of the exponent value obtained from several datasets: overall maps (Fig. 9), the Burum granite map at scale of 1/1500 (Fig. 9), and the refined micro-block map (Fig. 10a and b). Slope values for these multi-scale datasets are between 1.7 and 1.8 and are obtained over three orders of magnitude (10 m–10 km). This reveals

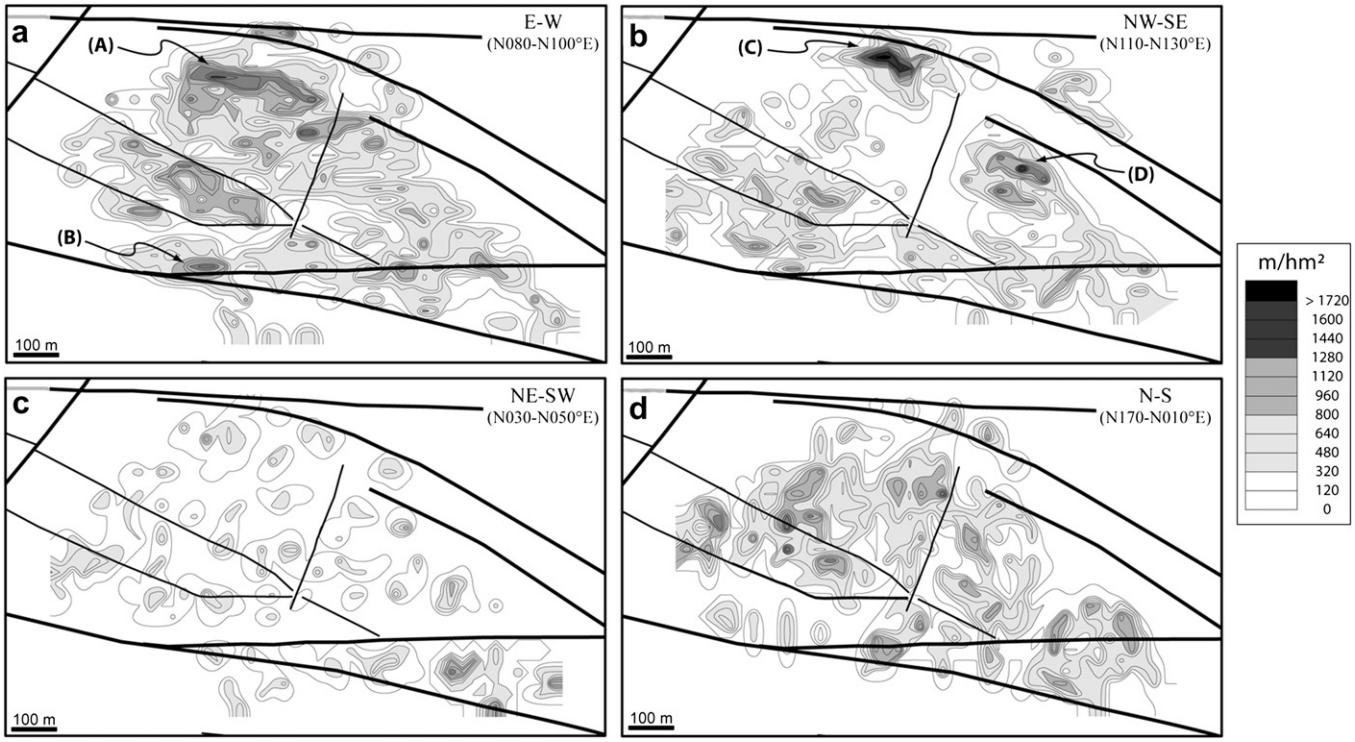

Fig. 14. Micro-block density maps according to families of lineament orientation: N–S (N170-010°E), NE–SW (N030-050°E), E–W (N080-100°E) and NW–SE (N110-130°E). We used a kernel of 25 m by 25 m (see text for more explanations). Main cluster zones a, b, c and d are shown.

that power-law trace-length distributions are consistent over large range of scales and that single measure of fractal dimension realized at a given scale can be extrapolated to other different scales. The principal application is in prediction of populations of sub-seismic faults from seismic data for hydrocarbon reservoir characterization.

8.2. Fractures networks transmissivity and dual porosity model

Fluid flow in fractured rocks depends on numerous parameters associated with the geometry of the fracture systems (i.e. length, orientation, spacing, spatial distribution, connectivity), the physical properties of the rock matrix (porosity, permeability), and the fracture aperture (stress state, roughness, channeling, sealing). This study focused on geometrical criteria from regional to outcrop scales. The role of the other parameters, which require analyses from outcrop to microscopic scales, has not been addressed here, but their influence will be briefly discussed later in this paper.

The trace-length distribution of fractures gives us a statistical tool for estimating the connectivity of fracture systems. Bour and Davy (1997) have shown that, for random 2D fracture patterns, the exponent a of the power-law length distribution has an important influence on the nature of connectivity. The exponent characterizes the relative abundance of fractures of different sizes. For exponents with $a > 3$, small fractures dominate the connectivity. For exponents $1 < a < 3$, both small and large fractures mainly affect the connectivity in a ratio which depends on a. Finally, if a is smaller than 1, the connectivity is influenced by the largest possible fractures. The Mukalla basement shows power-law trace-length distribution over three orders of magnitude (10–10000 m) with an exponent a equal to 1.8 (Fig. 9). The value of the exponent indicates that both relatively large and small fractures contribute to fluid flow and highlights the importance of the third order block size model described in Section 7 (Fig. 15b). This model shows that the connectivity of fracture systems is concentrated along tectonic systems (i.e. large fractures), but is also largely dependent on the joint systems (i.e. short fractures), as already proposed by Odling et al. (1999) for other cases.

The Mukalla basement fractured reservoir analog could therefore be defined as a reservoir-scale dual porosity model in terms of fracture transmissivity. On one hand, fault zones act as major conduits for fluid flow and correspond to the reservoir "backbone" (Fig. 15b), which is defined as all direct routes through the fracture network (Odling et al., 1999). On the other hand, joint systems can be considered as the reservoir matrix defined by a diffuse permeability affecting the whole rock mass (Fig. 15b). This suggests that, at a scale corresponding to the transition between tectonic and joint systems, there will be a change in the scaling behavior of fluid flow. The joint network of the matrix reservoir, when open, provides abundant continuous and homogeneously distributed pathways for fluid flow. The degree of connectivity of the matrix has important implications for fractured reservoir output because it controls the rate of fluid supply toward conduits. Fracture corridors highlighted during this study are localized at the transition between these two end-members (i.e. backbone and matrix), and could therefore optimize the fluid flow between them.

8.3. Reflection on production zones occurrences

Well data from geothermal and oil explorations in basement fractured reservoir reveal that fault zones are not systematically preferential conduits for fluid flow. In addition, if fluid supply in a fractured reservoir follows all potential conduits, then we should expected numerous distributed production zones of minor importance, and this is in contradiction with the localized major production zones observed in wells. Consequently, according to the well-connected fault zones network described in this study (i.e. "backbone") and an especially well-connected joint system (i.e. matrix) affecting the whole rock mass, we believe that fault zones

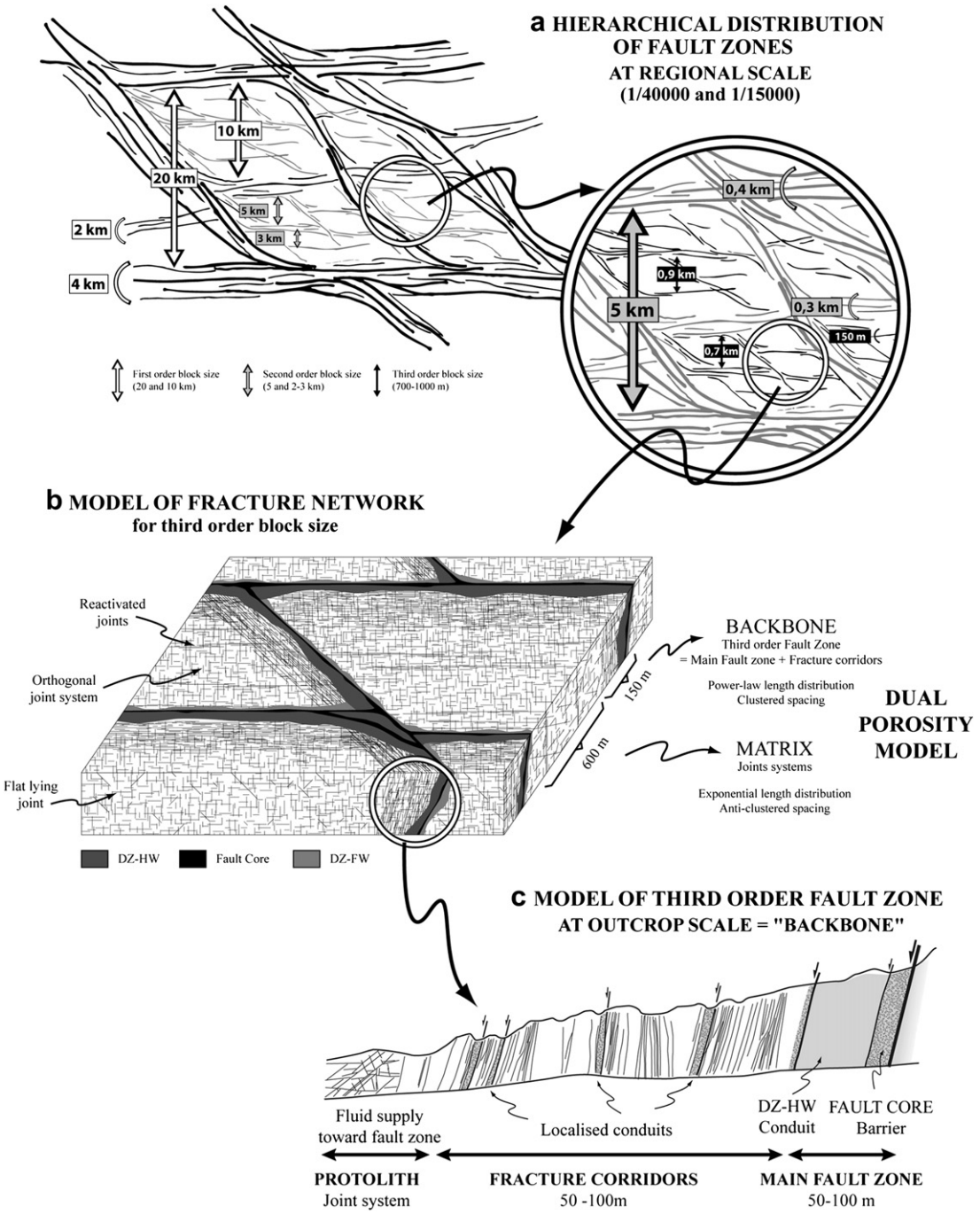

Fig. 15. Multi-scale model of fracture systems for the Mukalla basement and, more particularly, the Burum granite. (a) Model of fault zone network at regional scale. Arrows indicate characteristic block sizes of the hierarchical fault zone distribution model. Brackets highlight thicknesses of fault zones of each order. (b) Model of fracture network for third order block. Geometrical and reservoir properties are indicated on the right. (c) Model of fracture network for third order fault zone. DZ-HW: Damage Zone in the Hanging Wall; DZ-FW: Damage Zone in the Foot Wall.

probably possess further internal characteristics which can concentrate fluid flow making them useful production zones.

Concerning fault related fluid flow, Caine et al. (1996) have defined four end-members architectural styles according to the relative percentage of fault core and damage zone structures: localized conduits, distributed conduits, localized barriers, and combined conduit-barriers. In this model, damage zones act as conduits and fault cores act as barriers. Numerous field studies (Evans et al., 1997; Genter, 2000; Géraud et al., 2006; Micarelli et al., 2006) have confirmed this model. When a fault zone has been subjected to fluid flow, then alteration and precipitation could seal the fault core which will then act as an impermeable zone and a barrier, and subsequently, damage zones, and potentially the fracture corridors highlighted in this study, will be used for fluid flow.

A simpler way to concentrate fluid flow is to bring fluid in a conduit and to prevent it joining another nearby conduit through oblique structures and matrix network. In other words, we believe that production zones should have a combined conduit-barrier permeability structure as defined by Caine et al. (1996). Studies on

fractured reservoirs realized for industrial requirements show that production zones are often spatially associated with mineralization (e.g. calcite), and fracture clusters (e.g. Evans et al., 2005; Sausse et al., 2006; Ledésert et al., 2009). Furthermore, numerous natural examples show successive paleo-fluid circulations in the same deformation zone, emphasized by overprinted mineralization, showing that fault zone could be a zone of mechanical weakness which can be more easily activated. As a consequence, we think that a fault which has already undergone paleo-fluid circulation, and consequently alteration and/or precipitation, could be a preferential path for a next fluid flow. This spatial relationship can be interpreted as a sealed fault core (i.e. calcite mineralization) acting as a barrier and damage zone (i.e. fracture clusters) acting as a conduit.

9. Conclusions

Multi-scale mappings of fracture systems in the crystalline basement of Yemen have been described through statistical analyses of direction, length, spacing, density, and spatial distribution. These results, combined with field observations, have been used to model the geometry of the fracture networks in an analog basement rocks, from multi-kilometric to decametric scales. Model suggests that fractures observed at all scales (regional faults to joints) influence the degree of connectivity of the fractured reservoir and the fluid flow behavior.

1. The E–W and NW–SE extensional fault systems show a hierarchical organization of fault zone with characteristics parameters like length, thickness, and spacing. It presents a “self-similar” geometry characterized by an interlocking of parallelogram shaped structural blocks of different order.
2. The E–W and NW–SE extensional fault systems present evidence of fractal organization: (i) power-law trace-length distribution has been determined over three orders of magnitude (10–10000 m) with an exponent of 1.8, that reveals scale-invariant behavior, and (ii) we have demonstrated that tectonic systems show clustered spacing, while joint systems show anti-clustered spacing (i.e. random or regular spatial distribution).
3. When datasets are refined by orientation sets, the length population technique can potentially distinguish joint systems from tectonic systems and consequently is a useful tool for structural network interpretation. Tectonic systems show power-law trace-length distribution with exponent of 1.7, and seem to be scale-invariant. Joint systems show negative exponential trace-length distribution, and are restricted to a characteristic scale range.
4. E–W and NW–SE trending extensional faults are related to Jurassic and Cretaceous rifting, even if the latter is inherited from Pan-African orogeny (i.e. Nadj Fault reactivation). These structures were reactivated during the Gulf of Aden opening. On the regional scale (i.e. 1/40000 and 1/15000), NE–SW orientation sets can be interpreted as Cenozoic strike-slip faults corresponding to the onshore continuity of the Mukalla transform faults, while on the larger scale (i.e. 1/1500 and 1/500), NE–SW structures present evidence of a joint system. A typical orthogonal joint system comprised of N–S and E–W sets has been recognized in the Burum granite. Reactivation of the E–W trending joint set during Jurassic and Cretaceous rifting have been highlighted.
5. A basement fractured reservoir can be defined in a simpler way as a reservoir-scale dual porosity model. On the one hand, tectonic systems act as major conduits for fluid flow and correspond to the reservoir “backbone”. On the other hand, joint systems can be considered as reservoir matrix defines by a diffuse permeability affecting the whole rock mass. We believe that fault zones should have a combined conduit-barrier permeability structure as defined by Caine et al. (1996) in order to be a good production zone. As a consequence, a fault which has already undergone paleo-fluid circulation, and consequently alteration and/or precipitation, could be preferential zone for concentrating fluid flow.

Acknowledgments

We would like to thank the Block 10 partners in Yemen (Oxy, Kufpec, Sinochem and TOTAL) who have authorized this publication. A special thank to J.P. Gomez (TOTAL, Aberdeen) for his help in the understanding of the structural patterns in the Burum granite. The interpretation of the satellite images has been realized with the collaboration and the technical input of TOTAL Pau (thanks to J.P. Xavier) and TTI Production. We are also grateful to Joachim Place (ElfER, Germany) for data processing. The authors want also to thank R.W. Wilson and J.P. Turner for their valuable comments on the early versions of this manuscript, as well as N. Odling and J. Escuder Viruete for constructive reviews and Tom Blenkinsop for his editorial support.

References

Al-Saleh, A.M., Boyle, A.P., Mussett, A.E., 1998. Metamorphism and 40Ar/39Ar dating of the Halaban Ophiolite and associated units: evidence for two-stage orogenesis in the eastern Arabian shield. Journal of the Geological Society 155, 165–175.

Bellahsen, N., Fournier, M., d’Acremont, E., Leroy, S., Daniel, J.M., 2006. Fault reactivation and rift localization: northeastern Gulf of Aden margin. Tectonics 25. doi:10.1029/2004TC001626.

Beydoun, Z.R., As-Saruri, M.L., Baraba, R.S., 1996. Sedimentary basins of the Republic of Yemen: their structural evolution and geological characteristics. Revue de l’Institut Français du Pétrole 51, 763–775.

Birse, A.C.R., Bott, W.F., Morrison, J., Samuel, M.A., 1997. The Mesozoic and early Tertiary tectonic evolution of the Socotra area, eastern Gulf of Aden, Yemen. Marine and Petroleum Geology 14, 675–684.

Blasband, B., White, S., Brooijmans, P., De Boorder, H., Visser, W., 2000. Late proterozoic extensional collapse in the Arabian-Nubian shield. Journal of the Geological Society 157, 615–628.

Bonnet, E., Bour, O., Odling, N.E., Davy, P., Main, I., Cowie, P., Berkowitz, B., 2001. Scaling of fracture systems in geological media. Reviews of Geophysics 39, 347–383.

Bosence, D.W.J., 1997. Mesozoic rift basins of Yemen. Marine and Petroleum Geology 14, 611–616.

Bour, O., Davy, P., 1997. Connectivity of random fault networks following a power law fault length distribution. Water Resources Research 33, 1567–1583.

Bour, O., Davy, P., Darcel, C., Odling, N., 2002. A statistical scaling model for fracture network geometry, with validation on a multiscale mapping of a joint network (Hornelen Basin, Norway). Journal of Geophysical Research B: Solid Earth 107. doi:10.1029/2001JB000176.

Brannan, J., Gerdes, K.D., Newth, I.R., 1997. Tectono-stratigraphic development of the Qamar basin, Eastern Yemen. Marine and Petroleum Geology 14, 701–730.

Caine, J.S., Evans, J.P., Forster, C.B., 1996. Fault zone architecture and permeability structure. Geology 24, 1025–1028.

Castaing, C., Halawani, M.A., Gervais, F., Chilès, J.P., Genter, A., Bourgine, B., Ouillon, G., Brosse, J.M., Martin, P., Genna, A., Janjou, D., 1996. Scaling relationships in intraplate fracture systems related to Red Sea rifting. Tectonophysics 261, 291–314.

Chester, F.M., Evans, J.P., Biegel, R.L., 1993. Internal structure and weakening mechanisms of the San Andreas Fault. Journal of Geophysical Research 98, 771–786.

Childs, C., Manzocchi, T., Walsh, J.J., Bonson, C.G., Nicol, A., Schöpfer, M.P.J., 2009. A geometric model of fault zone and fault rock thickness variations. Journal of Structural Geology 31, 117–127.

Clark, R.M., Cox, S.J.D., 1996. A modern regression approach to determining fault displacement-length scaling relationships. Journal of Structural Geology 18, 147–152.

d’Acremont, E., Leroy, S., Maia, M., Patriat, P., Beslier, M.O., Bellahsen, N., FournierM., Gente, P., 2006. Structure and evolution of the eastern Gulf of Aden: insights from magnetic and gravity data (Encens-Sheba MD117 cruise). Geophysical Journal International 165, 786–803.

Dauteuil, O., Huchon, P., Quemeneur, F., Souriot, T., 2001. Propagation of an oblique spreading centre: the western Gulf of Aden. Tectonophysics 332, 423–442.

Ellis, A.C., Kerr, H.M., Cornwell, C.P., Williams, D.O., 1996. A tectono-stratigraphic framework for Yemen and its implications for hydrocarbon potential. Petroleum Geoscience 2, 29–42.

Evans, J.P., Forster, C.B., Goddard, J.V., 1997. Permeability of fault-related rocks, and implications for hydraulic structure of fault zones. Journal of Structural Geology 19, 1393–1404.
Evans, K.F., Genter, A., Sausse, J., 2005. Permeability creation and damage due to massive fluid injections into granite at 3.5 km at Soultz: 1. Borehole observations. Journal of Geophysical Research B Solid Earth 110, 1–19.
Faulkner, D.R., Lewis, A.C., Rutter, E.H., 2003. On the internal structure and mechanics of large strike-slip fault zones: field observations of the Carboneras fault in southeastern Spain. Tectonophysics 367, 235–251.
Géraud, Y., Diraison, M., Orellana, N., 2006. Fault zone geometry of a mature active normal fault: a potential high permeability channel (Pirgaki fault, Corinth rift, Greece). Tectonophysics 426, 61–76.
Géraud, Y., Rosener, M., Surma, F., Place, J., Le Garzic, E., Diraison, M., 2010. Physical properties of fault zones within a granite body: example of the Soultz-sous-Forêts geothermal site. Comptes Rendus Geoscience 342, 566–574.
GDR-surveying team and the Department of Geology & Mineral Exploration/Aden, 1987. Geological Map of Republic of Yemen (1:100 000).
Genter, A., 2000. Over 10 years of geological investigations within the HDR Soultz project, France. In: Proceedings, World Geothermal Congress 2000, Kyushu-Tohoku, Japan.
Genter, A., Castaing, C., 1997. Scale effects in the fracturing of granite. Effets d'échelle dans la fracturation des granites 325, 439–45.
Gillespie, P.A., Howard, C.B., Walsh, J.J., Watterson, J., 1993. Measurement and characterisation of spatial distributions of fractures. Tectonophysics 226, 113–141.
Holden, A., Kerr, H.M., 1997. A subsurface lithostratigraphic division of the Hauterivian to Aptian, Furt (informal) and Qishn formations, Yemen. Marine and Petroleum Geology 14, 631–642.
Huchon, P., Khanbari, K., 2003. Rotation of the syn-rift stress field of the northern Gulf of Aden margin, Yemen. Tectonophysics 364, 147–166.
Khanbari, K., 2000. Propagation d'un rift océanique: le Golfe d'Aden. Ses effets structuraux sur la marge Yéménite. Thèse de doctorat de l'Univeristé Paris-Sud (325 pages).
Kim, Y.-S., Peacock, D.C.P., Sanderson, D.J., 2004. Fault damage zones. Journal of Structural Geology 26, 503–517.
Ledésert, B., Dubois, J., Genter, A., Meunier, A., 1993a. Fractal analysis of fractures applied to Soultz-sous-Forets hot dry rock geothermal program. Journal of Volcanology and Geothermal Research 57, 1–17.
Ledésert, B., Dubois, J., Velde, B., Meunier, A., Genter, A., Badri, A., 1993b. Geometrical and fractal analysis of a three-dimensional hydrothermal vein network in a fractured granite. Journal of Volcanology and Geothermal Research 56, 267–280.
Ledésert, B., Hébert, R.L., Grall, C., Genter, A., Dezayes, C., Bartier, D., Gérard, A., 2009. Calcimetry as a useful tool for a better knowledge of flow pathways in the Soultz-sous-Forêts Enhanced Geothermal System. Journal of Volcanology and Geothermal Research 181, 106–114.
Lepvrier, C., Fournier, M., Bérard, T., Roger, J., 2002. Cenozoic extension in coastal Dhofar (southern Oman): implications on the oblique rifting of the Gulf of Aden. Tectonophysics 357, 279–293.
Leroy, S., Gente, P., Fournier, M., d'Acremont, E., Patriat, P., Beslier, M.O., Bellahsen, N., Maia, M., Blais, A., Perrot, J., Al-Kathiri, A., Merkouriev, S., Fleury, J.M., Ruellan, P.Y., Lepvrier, C., Huchon, P., 2004. From rifting to spreading in the eastern Gulf of Aden: a geophysical survey of a young oceanic basin from margin to margin. Terra Nova 16, 185–192.
Long, J.C.S., Witherspoon, P.A., 1985. The relationship of the degree of interconnection to permeability in fracture networks. Journal of Geophysical Research 90, 3087–3098.
Mandelbrot, B., 1972. The Fractal Geometry of Nature. W.H. Freeman and Company, New-York.
Manighetti, I., Tapponnier, P., Courtillot, V., Gruszow, S., Gillot, P.Y., 1997. Propagation of rifting along the Arabia-Somalia plate boundary: the Gulfs of Aden and Tadjoura. Journal of Geophysical Research B Solid Earth 102, 2681–2710.
McCaffrey, K.J.W., Sleight, J.M., Pugliese, S., Holdsworth, R.E., 2003. Fracture Formation and Evolution in Crystalline Rocks: Insights from Attribute Analysis. In: Geological Society, Special Publications, vol. 214 109–124.
Meert, J.G., 2003. A synopsis of events related to the assembly of eastern Gondwana. Tectonophysics 362, 1–40.
Micarelli, L., Moretti, I., Daniel, J.M., 2003. Structural properties of rift-related normal faults: the case study of the Gulf of Corinth, Greece. Journal of Geodynamics 36, 275–303.
Micarelli, L., Moretti, I., Jaubert, M., Moulouel, H., 2006. Fracture analysis in the south-western Corinth rift (Greece) and implications on fault hydraulic behavior. Tectonophysics 426, 31–59.
Odling, N.E., 1997. Scaling and connectivity of joint systems in sandstones from western Norway. Journal of Structural Geology 19, 1257–1271.
Odling, N.E., Gillespie, P., Bourgine, B., Castaing, C., Chilés, J.P., Christensen, N.P., Fillion, E., Genter, A., Olsen, C., Thrane, L., Trice, R., Aarseth, E., Walsh, J.J., Watterson, J., 1999. Variations in fracture system geometry and their implications for fluid flow in fractured hydrocarbon reservoirs. Petroleum Geoscience 5, 373–384.
Peacock, D.C.P., Knipe, R.J., Sanderson, D.J., 2000. Glossary of normal faults. Journal of Structural Geology 22, 291–305.
Pickering, G., Bull, J.M., Sanderson, D.J., 1995. Sampling power-law distributions. Tectonophysics 248, 1–20.
Price, N.J., Cosgrove, J.W., 1990. Analysis of Geological Structures. Cambridge University Press, p. 502.
Redfern, P., Jones, J.A., 1995. The interior rifts of Yemen - Analysis of basin structure and stratigraphy in a regional plate tectonic context. Basin Research 7, 337–356.
Sanders, C.A.E., Fullarton, L., Calvert, S., 2003. Modelling Fracture Systems in Extensional Crystalline Basement. In: Geological Society, Special Publications, vol. 214 221–236.
Sausse, J., Fourar, M., Genter, A., 2006. Permeability and alteration within the Soultz granite inferred from geophysical and flow log analysis. Geothermics 35, 544–560.
Schlische, R.W., Young, S.S., Ackermann, R.V., Gupta, A., 1996. Geometry and scaling relations of a population of very small rift-related normal faults. Geology 24, 683–686.
Schultz, R.A., Soliva, R., Fossen, H., Okubo, C.H., Reeves, D.M., 2008. Dependence of displacement-length scaling relations for fractures and deformation bands on the volumetric changes across them. Journal of Structural Geology 30, 1405–1411.
Schulz, S.E., Evans, J.P., 1998. Spatial variability in microscopic deformation and composition of the Punchbowl fault, southern California: implications for mechanisms, fluid-rock interaction, and fault morphology. Tectonophysics 295, 223–244.
Schutter, S.R., 2003. Occurrences of hydrocarbons in and around igneous rocks. In: Petford, N., McCaffrey, J.W. (Eds.), Hydrocarbons in Crystalline Rocks. Geological Society, London, Special Publications, vol. 214, pp. 35–68.
Stoeser, D.B., Camp, V.E., 1985. Pan-African microplate accretion of the Arabian shield. Geological Society of America Bulletin 96, 817–826.
Velde, B., Dubois, J., Moore, D., Touchard, G., 1991. Fractal patterns of fractures in granites. Earth and Planetary Science Letters 104, 25–35.
Escuder Viruete, J., Carbonell, R., Jurado, M.J., Jurado, M.J., Marti, D., Pérez-Estaun, A., 2001. Two-dimensional geostatistical modeling and prediction of the fracture system in the Albala Granitic Pluton, SW Iberian Massif, Spain. Journal of Structural Geology 23, 2011–2023.
Watchorn, F., Nichols, G.J., Bosence, D.W.J., 1998. Rift-related sedimentation and stratigraphy, southern Yemen (Gulf of Aden). In: Purser, B.H., Bosence, D.W.J. (Eds.), Sedimentation and Tectonics of Rift Basins: Red Sea-Gulf of Aden. Chapman & Hall, London, pp. 165–192.
Windley, B.F., Whitehouse, M.J., Ba-Bttat, M.A.O., 1996. Early Precambrian gneiss terranes and Pan-African island arcs in Yemen: crustal accretion of the eastern Arabian shield. Geology 24, 131–134.